JGR Planets

RESEARCH ARTICLE

10.1029/2025JE009404

Characterization of the Outer Uranian Rings in the Visual and Near-IR Using Keck, JWST, and HST Observations

Imke de Pater[1,2], Mark R. Showalter[3], Matt M. Hedman[4], Heidi B. Hammel[5], Mike Roman[6,7], Leigh N. Fletcher[6], Maryame El Moutamid[8], and Damya Souami[9,10]

[1]Department of Astronomy, University of California, Berkeley, CA, USA, [2]Department of Earth & Planetary Science, University of California, Berkeley, CA, USA, [3]SETI Institute, Mountain View, CA, USA, [4]Department of Physics, University of Idaho, Moscow, ID, USA, [5]Association of Universities for Research in Astronomy, Washington, DC, USA, [6]School of Physics and Astronomy, University of Leicester, Leicester, UK, [7]Facultad de Ingeniería y Ciencias, Universidad Adolfo Ibáñez, Santiago, Chile, [8]Southwest Research Institute, Boulder, CO, USA, [9]LIRA, CNRS UMR8254, Observatoire de Paris, Université PSL, Sorbonne Université, Université Paris Cité, France, [10]naXys, Department of Mathematics, University of Namur, Namur, Belgium

Key Points:

- Based upon its blue color, radial extent and spectral features, we infer that the μ ring must be composed of tiny icy grains
- The ν ring is red, and composed of grains rich in organics, like tholins
- The μ ring shows evidence of variability; in the Hubble Space Telescope data, it decreased in brightness by a factor of two between 2003 and 2006

Correspondence to:

I. de Pater,
imke@berkeley.edu

Citation:

de Pater, I., Showalter, M. R., Hedman, M. M., Hammel, H. B., Roman, M., Fletcher, L. N., et al. (2026). Characterization of the outer Uranian rings in the visual and near-IR using keck, JWST, and HST observations. *Journal of Geophysical Research: Planets*, *131*, e2025JE009404. https://doi.org/10.1029/2025JE009404

Received 20 AUG 2025
Accepted 9 MAR 2026

Author Contributions:

Conceptualization: Imke de Pater, Mark R. Showalter
Data curation: Imke de Pater, Mark R. Showalter, Heidi B. Hammel, Mike Roman, Leigh N. Fletcher, Maryame El Moutamid
Formal analysis: Imke de Pater, Mark R. Showalter, Matt M. Hedman
Funding acquisition: Imke de Pater, Mark R. Showalter
Investigation: Imke de Pater, Mark R. Showalter, Matt M. Hedman
Methodology: Imke de Pater, Mark R. Showalter, Matt M. Hedman
Project administration: Imke de Pater, Mark R. Showalter
Resources: Imke de Pater, Mark R. Showalter
Software: Imke de Pater, Mark R. Showalter, Matt M. Hedman
Supervision: Imke de Pater

Abstract We present observations of the Uranian outer ring system at near-infrared and visible wavelengths. Observations with the Keck Telescope were taken in July-August 2007 at 2.12 and 1.63 μm, when the ring plane was almost edge-on (ring opening angle $B = 0.62$–$0.24°$). These data showed, for the first time, the μ ring at infrared wavelengths. NIRCam on the James Webb Space Telescope observed Uranus in 2023–2025 at wavelengths 1.4–4.8 μm and $B \sim 60$–$65°$. Hubble Space Telescope data were obtained between 2003 and 2013 at wavelengths 0.45–0.96 μm and B from $-17°$ to $+25°$. We confirm that the μ ring is blue and the ν ring red. Both rings show strong absorption bands at 3 μm; the μ ring also shows an emission peak at 3.6 μm. Based upon a combination of the spectral slope and absorption/emission features, the μ ring must be composed of (sub-)micron-sized icy grains. The ν ring is a dusty ring rich in organics (~10%–15% tholins). The radial profile of both rings is triangular, with an outward extension for the ν ring and inward for the μ ring. Both rings are optically thin; at 1.5 μm $\tau_0 \approx 10^{-5}$ for the μ ring and 3×10^{-5} for the ν ring. Based upon the composition and radial extent of the rings we suggest the μ ring to originate via micrometeoroid impacts on the icy moon Mab, and the ν ring via collisions between, and micrometeoroid impacts on, parent non-icy bodies embedded within this ring.

Plain Language Summary We present observations of the Uranian outer ring system, the μ and ν rings, at visible and near-infrared wavelengths. The observations were obtained with the Hubble Space Telescope, Keck and the James Webb Space Telescope at different ring opening angles, from almost "open" ($\sim 60°$) to essentially edge-on ($\sim 0.24°$). We confirm that the μ ring is blue and the ν ring red. A blue color is indicative of Rayleigh scattering, that is, the presence of (sub-)micron-sized particles, while a red color is the telltale sign of a dusty ring. Both rings show a strong absorption band near 3 μm, but the spectra look different longwards of this absorption feature. The μ ring spectrum is very similar to that of water-ice, while the ν ring spectrum resembles a rocky composition mixed in with ~10%–15% organic material, analogous to tholins. Both rings are optically thin. We suggest that the μ ring has been formed through micrometeoroid impacts on the icy moon Mab, liberating the tiny icy grains that make up this ring. The ν ring, like typical dusty rings, is sourced from collisions between, and micrometeoroid impacts on, larger but as yet unseen parent bodies orbiting within this ring. These bodies must be composed in part of organic materials.

1. Introduction

Uranus is surrounded by two sets of rings: *i*) The main ring system is comprised of the dusty ζ ring interior to 41,350 km (distance from the planet's center), and at increasing distances from the planet the 6, 5, 4, $\alpha, \beta, \eta, \gamma, \delta, \lambda$, and ϵ rings, the latter at a planetocentric distance of 51,149 km. *ii*) The outer ring system consists of two dusty rings: the ν ring at ~67,000 km and the μ ring at ~90,000 km. This outer ring system was discovered by Showalter and Lissauer (2006) in data from the Hubble Space Telescope (HST); a subsequent follow-up search in Voyager images (in the same paper) revealed both rings in forward-scattered light. Since the rings were brighter in forward-than back-scattered light, the authors suggested the rings to consist primarily of micron-sized dust. Soon after this discovery, de Pater, Hammel, et al. (2006), using data from the W. M. Keck Telescope, showed that the μ

Validation: Imke de Pater, Mark R. Showalter, Matt M. Hedman
Visualization: Imke de Pater, Mark R. Showalter
Writing – original draft: Imke de Pater, Mark R. Showalter
Writing – review & editing: Imke de Pater, Mark R. Showalter, Matt M. Hedman, Heidi B. Hammel, Mike Roman, Leigh N. Fletcher, Maryame El Moutamid, Damya Souami

ring appeared to be as blue as Saturn's *E* ring, while the ν ring showed a good resemblance to the red color of Saturn's *G* ring. The latter conclusions were derived from observations at 2.2 μm with the Keck telescope in August and October 2005, when the ring's inclination angles were 8.4° and 10.5°, respectively. The ν ring was detected quite easily after integrating over about an hour, but the μ ring remained invisible; instead of a detection, the authors derived a 3-σ upper limit for this ring at 2.12 μm, which revealed its blue color. Such a spectral slope suggests a steep size distribution, dominated by micron and submicron sized grains.

A unique opportunity presented itself in May–August of 2007, when the Earth moved through the uranian ring plane (Ring Place Crossing, or RPX). During such times, optically thick rings will "vanish," while optically thin dusty rings will brighten considerably, since the path length along the line-of-sight through the rings increases by $1/\sin(B)$, with B the ring opening angle. A first paper on the RPX near-infrared Keck observing campaign focused on the main rings was published in 2007 (de Pater et al., 2007); the full data set for Uranus's main ring system (including data from the Nasmyth adaptive optics (AO) System—Near-Infrared Imager and Spectrograph NACO on the Very Large Telescope, VLT) was published in 2013 (de Pater et al., 2013). In the present paper, we present results focused on the Uranian outer ring system using a subset of the observations conducted with the Keck telescope in July-August 2007. These data show for the first time the μ ring at infrared wavelengths, and confirm its blue color.

More recently, after the launch of the James Webb Space Telescope (JWST) (Gardner et al., 2023), the Uranian system was imaged several times with the Near-Infrared Camera NIRCam (Huff, 2005; M. J. Rieke et al., 2023); many of these images reveal the planet's outer ring system at several wavelengths between 1 and 5 μm, confirming the spectral slopes of these rings. Most excitingly, they show spectral features in the 3–4 μm wavelength range which reveal their composition. By augmenting the infrared Keck/NIRC2 and JWST/NIRCam observations with multi-wavelength visible-light images from the Hubble Space Telescope (HST), taken between 2003 and 2013, we built a database that covers the rings at wavelengths from ∼0.5 μm to ∼5 μm. Hence, this study represents the most comprehensive characterization of the outer Uranian rings to date.

In Section 2 we present the data, split in three subsections covering the Keck, JWST/NIRCam, and HST data. Section 3 presents the results from each telescope in its separate subsection. The data are combined in Section 4, where we discuss the spectra, optical depth, shape and orbits of the rings, and their origins. Section 5 summarizes our conclusions.

2. Observations and Data Reduction

2.1. Keck/NIRC2

We observed the outer ring system of Uranus with the Keck telescope on UT 26 and 27 July, and 8 and 9 August 2007. The rings were almost edge-on at a ring opening angle $B = 0.61°$ in July and $B \sim 0.25°$ in August. The subsolar latitude was $-1.42°$ in July ($-1.34°$ in August), so that we observed the unlit side of the rings, that is, we only detected transmitted (though still backscattered) light. We imaged Uranus with the infrared detector NIRC2, a 1024 × 1024 Aladdin-3 InSb array. We used the NARROW camera at 9.94 ± 0.03 mas/pixel (de Pater, Gibbard, & Hammel, 2006), which translates into 139.6 km/pixel at Uranus' distance in July, and 138.6 km/pixel in August. NIRC2 was coupled to the AO system (Wizinowich et al., 2000), and we used the planet Uranus itself for wavefront sensing (van Dam et al., 2004; van Dam & Macintosh, 2003) to achieve an angular resolution at 2 μm near the diffraction limit of the telescope, ∼45 mas (∼630 km at Uranus). The first three sets of observations were carried out in the K′ band, centered at a wavelength of 2.124 μm. At this wavelength, sunlight is absorbed by methane and hydrogen gas in Uranus's atmosphere, greatly reducing scattered light from the planet. The observations on August 9 were conducted in the H band, centered at 1.63 μm. The observations are summarized in Table 1.

All images were processed using standard near-infrared data reduction techniques (flat-fielded, sky-subtracted, with bad pixels replaced by the median of surrounding pixels). The geometric distortion in the Keck images was corrected using the "dewarp" routines provided by Brian Cameron of the California Institute of Technology (https://www2.keck.hawaii.edu/inst/nirc2/dewarp.html), and the images needed to be rotated by ∼0.25° clockwise to align the rings perfectly north-south on the detector. On July 26, August 8, and August 9, the north (on the sky) side of the ring system was observed. On July 27, we observed the south side to avoid contamination of the bright moons (Miranda in this case). It is not possible, however, to avoid the smaller moons in the Uranian system,

Table 1
Keck/NIRC2 Observations of the μ and ν Rings of Uranus (in 2007)

Date/time (UT) 2007	Wavelength (μm)	N[a]	B[b] (deg)	B_0[b] (deg)	Ring[c] (N/S)	α[d] (deg)	Δ[e] (AU)	$r_\odot$[f] (AU)	Pixel size (km)
July 26 ∼11–15	K' (1.95–2.30)	36	0.62	−1.42	N	2.06	19.36	20.09	139.60
July 27 ∼11–15	K' (1.95–2.30)	32	0.60	−1.41	S	2.02	19.35	20.09	139.60
August 08 ∼11–15	K' (1.95–2.30)	48	0.27	−1.34	N	1.55	19.23	20.09	138.65
August 09 ∼11–14	H (1.49–1.78)	44	0.24	−1.33	N	1.51	19.22	20.09	138.59

[a] # frames: 2 min per frame in K'; 1 min per frame in H band. [b] B and B_0 are the apparent ring opening angles (in degrees) as seen from Earth and the Sun. [c] Side of the ring imaged; north (N) or south (S) of Uranus. [d] α is the solar phase angle. [e] Geocentric distance. [f] Heliocentric distance.

and since the rings were essentially edge-on, these small moons seemed to move "through" the rings, since they may be in front, behind, or in-between rings while orbiting the planet in essentially the same plane as the rings. Examples are shown in Figure 1. Since the locations of moons were different in each frame, we had to remove the moons individually from each frame before combining the images. In the K′ band, the number of frames per day varied from 32 to 48 frames, each with an integration time of 2 min; in H band (August 9), we used 44 frames of 1 min each. On that day, there were too many small moons interfering with the data on the south side to create clean images, so we only use the data taken on the north side. To increase the signal-to-noise ratio (SNR), we assumed the rings on July 26 and 27 to be symmetric north and south, and mirrored the ring before averaging the data on these 2 dates.

After careful calibration of the data (de Pater et al., 2013), all data were converted to the dimensionless parameter I/F, where I is the reflected intensity and πF the solar flux density at Uranus's distance (Hammel et al., 1989):

$$\frac{I}{F} = \frac{r_\odot^2 F_U}{\Omega F_{\mathrm{Sun}}}, \tag{1}$$

where $r_\odot$ is Uranus's heliocentric distance, and πF_{Sun} is the Sun's flux density at Earth's orbit (Colina et al., 1996), as observed in the relevant filters. The solid angle Ω is the pixel size of the NIRC2 camera in steradians. F_U is the observed flux density from Uranus and its ring system.

The results are shown in Figures 2 and 3: Figure 2 shows a close-up of the outer rings on one side of Uranus, and Figure 3 shows the entire ring system on July 26/27.

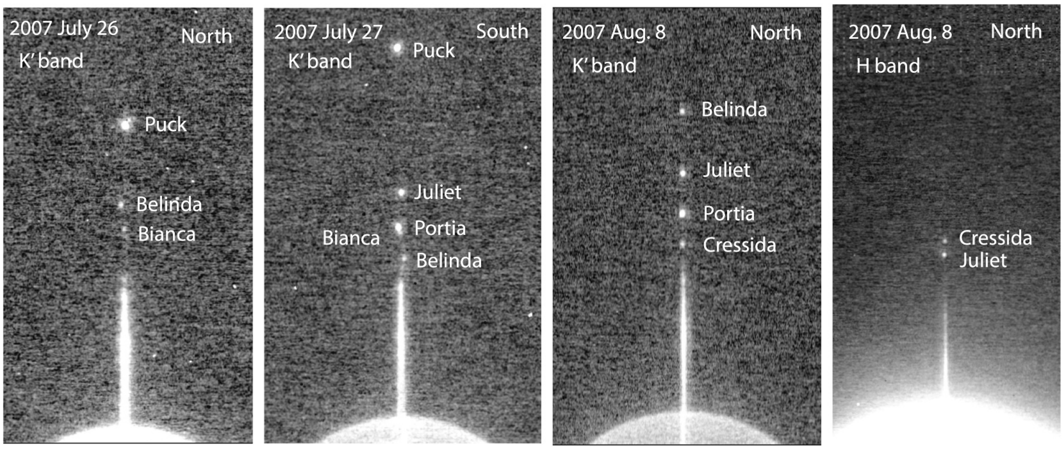

Figure 1. Keck: Uranus ring system in 2007 as observed in K′ and H bands on July 26, 27, August 8 and 9. These are single frames before the moonlets were subtracted. The moons orbit within the ring system, so their locations differ in each frame. The images are displayed with IDL's ATV, using asinh (inverse hyperbolic sine) scaling (Lupton et al., 1999) so one can see the faint rings next to bright Uranus.

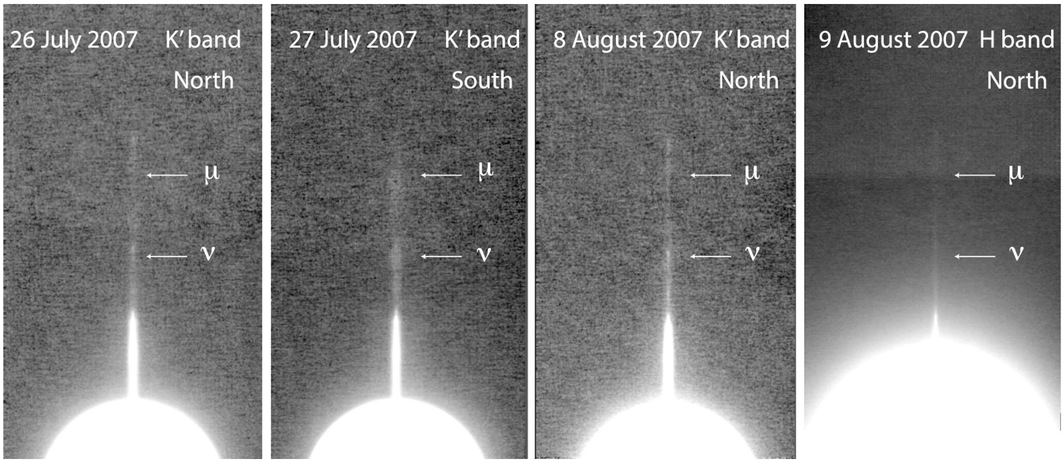

Figure 2. Keck: Uranus ring system in 2007 as observed in K′ and H bands on July 26, 27, August 8 and 9, after the moons (Figure 1) were subtracted from each frame and the images were combined. On July 26, August 8 and 9, only the north side of the rings were imaged; on July 27 only the south side was imaged, as indicated on the figure. The different gradations and apparent jumps in the background (horizontal lines) are caused by averaging frames with different sizes and integration times. The images are displayed with IDL's ATV, with the asinh scaling (as in Figure 1).

2.2. JWST/NIRCam

A total of three sets of observations were acquired with the Near-Infrared Camera NIRCam on the JWST. The first set was obtained as part of the Cycle 1 Outreach Campaign, Director's Discretionary program #2739 (PI: Klaus M. Pontoppidan). These observations were conducted in 2023 on UT 6 February and on 4–5 September. The observations were taken using the short wavelength filters F140M and F210M, paired (i.e., taken simultaneously) with the long wavelength filters F300M and F460M. (Note that the three-digit number in the middle of each NIRCam filter name refers to 100 times the approximate center wavelength of the filter in microns; the name ends with “‘M” for medium, “W” for wide, and “W2” for extra-wide.) The RAPID readout pattern was used with 8 groups per integration and a 5-point dither pattern, with an effective exposure time of 1825 s per filter. On Feb. 6 a fraction of only the F140M and F300M filters was successful, with an effective exposure time of 343 s.

The Observatory Scheduling Software (OSS) used was version 8.7. The raw (suffix “uncal.fits”) data were calibrated with the pipeline version 1.11.4, and Calibration References Data System (CRDS) (Bushouse et al., 2012; Greenfield & Miller, 2016) files CRDS–VER = 11.17.2 and CRDS–CTX = jwst-1149.pmap. The dithers were combined by the pipeline to produce the geometrically corrected “i2d.fits” files used in our analysis. We note that several steps in the data processing removes moons orbiting Uranus. Since we are interested in the outer ring system which we expect to be stable during the observing sequence (i.e., not move with respect to Uranus), the removal of moons helps to suppress the background. (For details on JWST data reduction, see: https://jwst-docs.stsci.edu/getting-started-with-jwst-data#gsc.tab=0).

A second set of JWST/NIRCam observations was obtained under GTO program #2768 (PI: Naomi Rowe-Gurney). Three sets of observations were acquired in 2024, on February 6–7, spread over a 36-hr period, that is, roughly two planet rotations. The observations were taken using the short wavelength filters F182M and F210M, paired with the long wavelength filters F410M and F480M. The dithers were combined by the pipeline to produce the i2d.fits files. The RAPID readout pattern was used with 10 groups per integration, yielding an effective exposure time of 535 s per filter for each of the three images. For these data the OSS used was version 9.1. The raw data were calibrated with the pipeline version 1.12.5, with CRDS files CRDS–VER = 11.17.6 and CRDS–CTX = jwst-1188.pmap. The dithers were combined by the pipeline to produce the i2d.fits files. We median-averaged the three images in each filter, which quite effectively removed moons orbiting Uranus, so that we obtained a relatively clean data set to analyze the outer ring system.

A third data set was obtained in 2025, on February 2, under GO program #6379 (PI: Maryame El Moutamid). These observations were focused on obtaining deep exposures of the planet's environment using the broad F150W2 filter paired with F322W2. The BRIGHT1 readout pattern was used, with ten groups per integration and

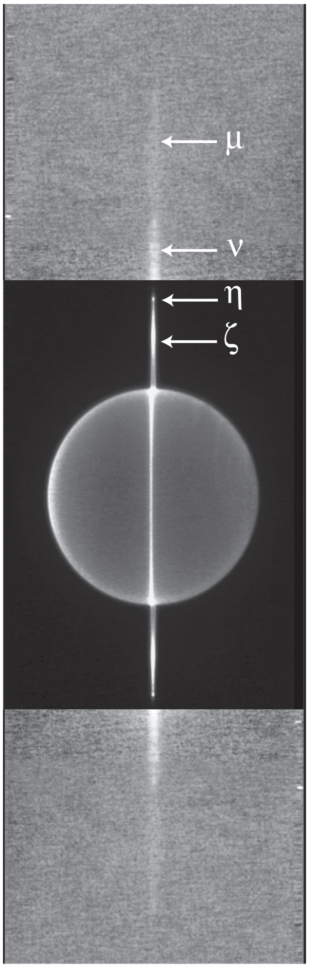

Figure 3. Keck: Uranus ring system as observed on 26 and 27 July 2007. The rings were assumed to be symmetric, and were mirrored north-south, before averaging. The inset is displayed at a different intensity scale to enable identification of details of the inner ring system.

ten integrations for each of the two consecutive visits. We used very small dithers so Uranus stayed at the same position to avoid persistent charge from the planet on the detector at locations outside the planet. This resulted in an effective exposure time of 5.66 hr. In addition, we used the short-wavelength broad filters F150W, F115W, and F070W, paired with the long-wavelength filters F356W, F444W, and F277W, each with an effective exposure time of ∼35 minutes. For these observations the OSS used was version 10.1. The uncal data were calibrated with the pipeline version 1.16.1, with CRDS files CRDS–VER = 12.0.5 and CRDS–CTX = jwst-1303.pmap. We used the final system-produced i2d.fits files for our analysis, which essentially removed all moons from the final images (since they move); we could use the system-produced images because we are only interested in the faint (assumed stable) outer ring system.

The combination of the three programs provided more wavelengths to characterize the spectra of the outer rings. Moreover, the third data set was taken in broader filters providing a higher SNR compared to the first two data sets.

The pixel size for the short wavelength filters is ∼0.0307″, which is ∼430–440 km at Uranus's distance from JWST. At long wavelengths the pixel size is ∼0.063″, or ∼880–900 km at Uranus's distance. This pixel size was matched to a Nyquist sampling (2 pixels over a full width at half maximum intensity, FWHM) at 2 and 4 μm for the short and long wavelengths, respectively. Hence, at shorter wavelengths the data are under-sampled. The observations are summarized in Table 2.

Although the field of view is 2.2′ × 2.2′, we are only interested in the tiny fraction of the image that contains Uranus and its ring system. The full image from February 2023 was used in the Public Outreach released image https://webbtelescope.org/. Because we are interested in the very faint outer ring system, the background must be as clean as possible. We were able to remove much, but not all, of the horizontal striping pattern that was present in the original outreach and GTO images. Our results for the Uranian system, focused on the outer ring system, are shown for all filters in Figure 4.

The data were converted to the dimensionless parameter I/F using Equation 1, with the solar flux as tabulated in G. H. Rieke et al. (2008). There is essentially no difference in the solar flux density as tabulated in the overlapping 1–2.4 μm range between Colina et al. (1996) and the above spectrum.

2.3. HST

Deep imaging of the Uranus system during 2003–2006 revealed a number of new aspects of the system, including two moons (Cupid and Mab) and the outer μ and ν rings (Showalter & Lissauer, 2006). A combination of the high-throughput “CLEAR” filter on the High Resolution Channel (HRC) of the Advanced Camera for Surveys (ACS), plus extensive co-adding of extremely long exposures (up to 250 s), were required to bring these features to light. Because of the ACS failure in 2006, observations of the 2007 RPX employed the older and less powerful Wide Field/Planetary Camera 2 (WFPC2). The Wide Field Camera 3 was installed in early 2009 and since then, all of HST's visual and near-IR imaging of Uranus has been performed using that instrument. For this paper, we have analyzed all of HST's images of the Uranus system 2003–2013 that had relatively long exposures through relatively wide filters (Table 3). Most subsequent observations of Uranus with HST have been focused on the atmosphere (cf. Simon et al. (2015)), and lack sufficient SNR for studies of the outer rings. Narrow filters and short exposures are not useful for this investigation because the rings are too faint. The selected images cover the wavelength range 0.45–0.96 μm, complementing the IR wavelengths observed by the Keck Telescope and JWST.

Figure 5 (top-row) shows examples of images from each of the HST instruments used in this analysis. In each case, the extreme (but intentional) saturation of the planet leads to a vertical “bloom” of white pixels, which

Table 2
JWST/NIRCam Observations of the Uranian System in 2023–2025

Proposal #—Date/time (UT) day/hr:min–day/hr:min	Filter	Wavelength (μm)	B^a (deg)	B^a_0 (deg)	α^b (deg)	Δ^c (AU)	$r^d_\odot$ (AU)	Pixel size (km)
#2739–6 February 2023:								
6/05:30–6/05:45	F140M	1.33–1.48	56.32	59.14	2.90	19.66	19.67	438
6/05:30–6/05:45	F300M	2.83–3.16	56.32	59.14	2.90	19.66	19.67	898
#2739–4–5 September 2023:								
4/22:10–4/23:34	F140M	1.33–1.48	64.11	61.40	2.81	19.28	19.63	430
4/22:10–4/23:34	F300M	2.83–3.16	64.11	61.40	2.81	19.28	19.63	881
4/22:34–5/00:15	F210M	1.99–2.20	64.11	61.40	2.81	19.28	19.63	430
4/22:34–5/00:15	F460M	4.52–4.75	64.11	61.40	2.81	19.28	19.63	881
#2768–6–7 February 2024:								
6/06:02–6/06:22	F182M	1.72–1.97	60.28	63.07	2.90	19.54	19.61	436
6/06:02–6/06:22	F480M	4.66–4.97	60.28	63.07	2.90	19.54	19.61	893
6/05:36–6/05:57	F210M	1.99–2.20	60.28	63.07	2.90	19.54	19.61	436
6/05:36–6/05:57	F410M	3.87–4.30	60.28	63.07	2.90	19.54	19.61	893
7/01:24–7/01:45	F182M	1.72–1.97	60.28	63.07	2.90	19.55	19.61	436
7/01:24–7/01:45	F480M	4.66–4.97	60.28	63.07	2.90	19.55	19.61	893
7/00:59–7/01:19	F210M	1.99–2.20	60.28	63.07	2.90	19.55	19.61	436
7/00:59–7/01:19	F410M	3.87–4.30	60.28	63.07	2.90	19.55	19.61	893
7/17:06–7/17:27	F182M	1.72–1.97	60.28	63.07	2.90	19.56	19.61	436
7/17:06–7/17:27	F480M	4.66–4.97	60.28	63.07	2.90	19.56	19.61	893
7/16:40–7/17:01	F210M	1.99–2.20	60.28	63.07	2.90	19.56	19.61	436
7/16:40–7/17:01	F410M	3.87–4.30	60.28	63.07	2.90	19.56	19.61	893
#6379–2 February 2025:								
2/01:05–2/07:30	F150W2	1.007–2.38	64.21	66.94	2.87	19.35	19.55	431
2/01:05–2/07:30	F322W2	2.432–4.013	64.21	66.94	2.87	19.35	19.55	877
2/07:49–2/08:27	F150W	1.331–1.668	64.21	66.94	2.87	19.35	19.55	431
2/07:49–2/08:27	F356W	3.136–3.981	64.21	66.94	2.87	19.35	19.55	877
2/08:33–2/09:08	F115W	1.013–1.282	64.21	66.94	2.87	19.35	19.55	431
2/08:33–2/09:08	F444W	3.881–4.982	64.21	66.94	2.87	19.35	19.55	877
2/09:13–2/09:51	F070W	0.624–0.781	64.21	66.94	2.87	19.35	19.55	431
2/09:13–2/09:51	F277W	2.422–3.131	64.21	66.94	2.87	19.35	19.55	877

[a] B and B_0 are the apparent ring opening angles (in degrees) as seen from JWST and the Sun. [b] α is the solar phase angle. [c] JWST-Uranus distance. [d] Heliocentric distance.

obscures the planet entirely. The images also illustrate the prominent glare pattern surrounding Uranus, which is much brighter than the rings we wish to study. This pattern is caused by the long tail of the point spread function (PSF) convolved with Uranus's bright disk. Without further processing, the rings are obscured, although multiple moons are visible.

All analysis was performed using images that were calibrated to physical units of intensity by the HST pipeline; all ACS and UVIS files have“flt” or “flc” suffixes, whereas all WFPC2 files have “c0m” suffixes. We converted from these units to I/F using Equation 1. These images are not geometrically corrected, but the World Coordinate System (Greisen & Calabretta, 2002) parameters provided by the pipeline enabled us to obtain an accurate mapping between pixel coordinates and lines of sight in J2000 (RA, dec) coordinates.

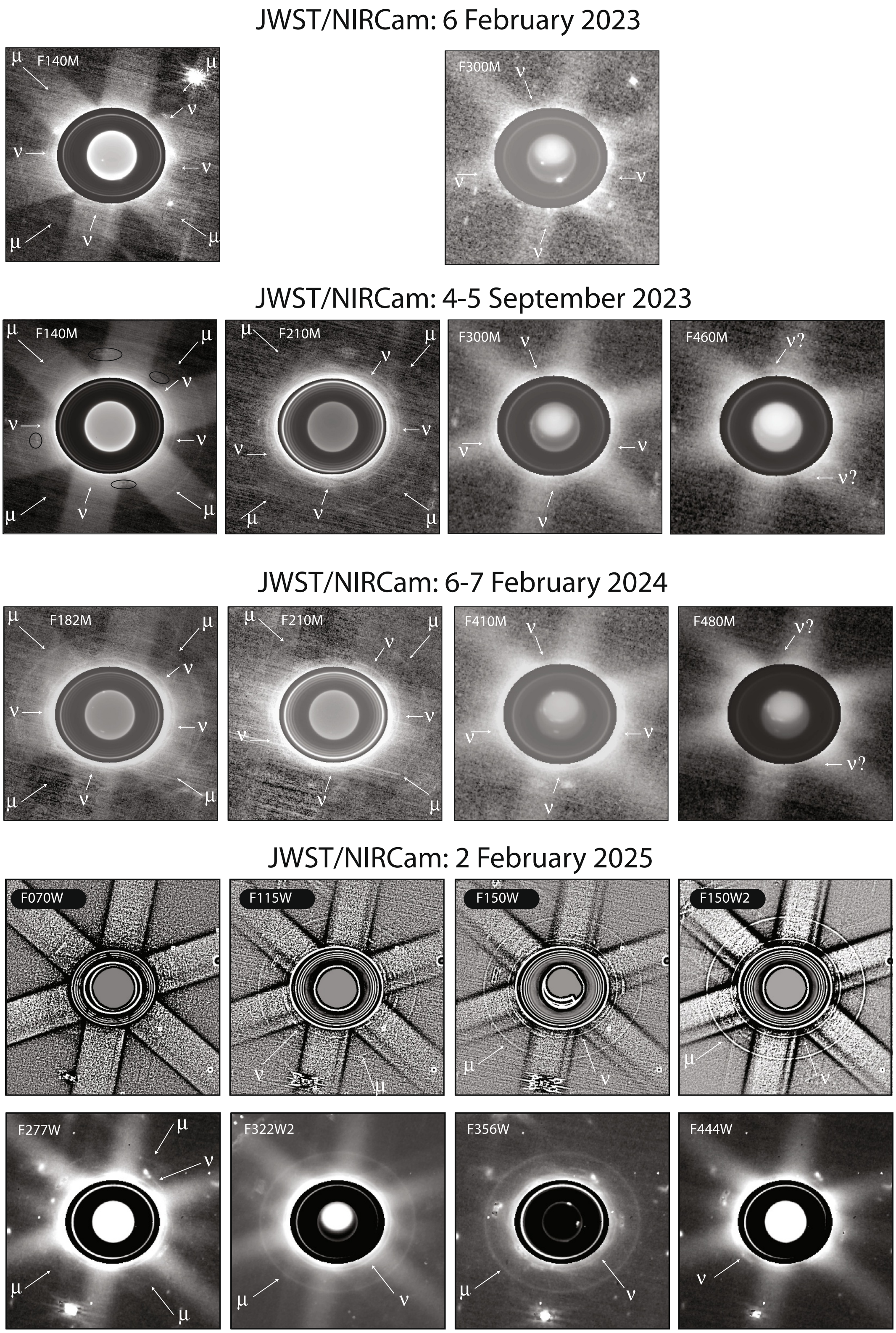
JWST/NIRCam: 6 February 2023
F140M
F300M
JWST/NIRCam: 4-5 September 2023
F140M
F210M
F300M
F460M
JWST/NIRCam: 6-7 February 2024
F182M
F210M
F410M
F480M
JWST/NIRCam: 2 February 2025
F070W
F115W
F150W
F150W2
F277W
F322W2
F356W
F444W
μ
ν
ν?

Figure 4.

We need to co-add large numbers of images to obtain quantitative results about the outer Uranian rings. Also, because Uranus is exceedingly bright at these wavelengths, we had to develop some new procedures to suppress the intense glare from the planet, which otherwise swamps the μ and ν rings. Our procedure involved the following steps.

1. We used SPICE tools (C. H. Acton, 1996; C. Acton et al., 2018) to predict the location of the brighter Uranian moons in each image, and then used the moons' measured locations to determine the correct center location of Uranus within each image. This compensated for the small offset between the predicted and actual locations of Uranus within each frame.
2. We grouped HST observations by orbit and filter. Each orbit of HST around Earth provides ~45 minutes of uninterrupted observing. For each group, we shifted the center of Uranus to a common location and then obtained the median of the set. This step improves SNR, while also suppressing the cosmic ray hits and other blemishes that do not correlate from one exposure to the next. At this step, we also obtained a mask identifying all the pixels that the HST processing pipeline identified as being hot or corrupted; masked pixels were excluded from further analysis. The middle row in Figure 5 shows the median-filtered versions from the top row.
3. Critically, we need to model the background glare pattern so that it can be subtracted from our median-filtered images. To meet this challenge, we took advantage of the fact that, at visual wavelengths, the glare pattern surrounding Uranus is quite stable among images from the same instrument and filter, and always at a fixed orientation on the detector, even when those images come from different years and regardless of the planet's orientation on the sky. For each instrument and filter, we constructed a global median image encompassing all observed ring opening angles and orientations. Upon subtracting the median image from each orbit-specific set, the outer rings finally come into view, as shown in the bottom row of Figure 5. Although some significant background variations still remain, more than 99% of the glare has been removed.

However, a straightforward global median of all the images through each filter does not quite meet our needs, because it also contains contributions from the outer rings. As a result, a subtraction of the global median will partially cancel out the rings we seek. We have developed a more careful approach, which ensures that the rings do not make any significant contribution to the model glare image we use for subtraction. The steps are illustrated in Figure 6. The first four panels show example images from individual orbits, in which the known radial boundaries of the outer rings are masked out in black (along with the pixels previously identified as masked). Notably, the black rings have different opening angles and, more subtly, different orientations on the sky. Using these masks, we can construct a *weighted* global median image, in which pixels that intercept one of the rings do not contribute. This image is shown at lower left. You can see a few small areas of black, particularly near the μ ring's ansa, that were never sampled in the absence of a ring. As a last step, a gaussian filter eliminates these and provides a suitable model for the glare. We note that we ignored variations in the solar phase angle, which should be OK since this angle is always less than 3° and we do not expect a steep opposition curve for dusty rings.

3. Results

3.1. Definitions and Procedures

Our goal is to obtain consistent photometry of the rings from all these data sets, which requires that we present our measurements in a consistent way. The quantity we use is the normal equivalent width (NEW), defined as:

Figure 4. JWST: Uranus outer ring system as imaged with James Webb Space Telescope, programs #2739 (top 2 rows), #2768 (third row), and #6379 in the two bottom rows. The filters are indicated on each panel. Uranus's north pole as projected on the sky is approximately up in these figures. In most filters the diffraction pattern of Uranus is quite visible, but nevertheless the μ and ν rings can be distinguished in several filters. Both rings are indicated by arrows. To visualize the outer rings as well as Uranus and its main ring system, we artificially diminished the intensity of Uranus and its main rings by factors of 250 (F140M), 400 (F182M), 100 (F210M), 500 (F300M), 700 (F410M), 200 (F460M), 500 (F480M), 20 (F444W), 30 (F356W), 50 (F277W), 100 (F322W2, F150W, F150W2), 50 (F115W), and 300 (F070W), separated by the dark ellipse just outside the ϵ ring. The images are displayed on a log scale. Some blemishes caused by imperfect moon removal in the #2739 images are circled in the F140M filter. Since 3 sets, separated by many hours, of the #2768 images were median averaged, the moons (but not the stars) were efficiently removed from these images since their locations varied from image to image. The #6379 observations were all obtained in Wide filters, such that at the short wavelengths scattered light from Uranus and the main rings overwhelmed the μ and ν rings. We therefore put these images through a low-pass filter by subtracting a smoothed copy of the image using a 10-pixel boxcar filter to make the outer rings visible (Image–smooth[Image,10] in IDL). At the longer W-filters one can see several moonlets; these all have been removed quite efficiently in the W2-filters, since these were integrated over 5.66 hr.

Table 3
HST Observations of the Rings of Uranus in 2003–2013

Instr/Filter[a]	Wavelength µm (+range in µm)	UT date begin yr-month-date	UT date end yr-month-date	B[b] (deg)	B_0[b] (deg)	N[c]	Exp. Times seconds
ACS/HRC/CLEAR	0.562 (0.413–0.823)	2003-08-25	2006-09-05	−17.4 to −5.1	−17.3 to −5.1	159	200–250
ACS/HRC/F475W	0.477 (0.423–0.534)	2003-08-25	2006-09-05	−17.4 to −5.1	−17.3 to −5.1	38	110–150
ACS/HRC/F606W	0.579 (0.479–0.680)	2003-07-12	2006-09-05	−17.4 to −5.1	−17.3 to −5.1	38	80–120
ACS/HRC/F775W	0.761 (0.710–0.828)	2005-08-27	2006-08-24	−9.0 to −4.6	−9.2 to −5.2	17	46–80
ACS/HRC/F814W	0.797 (0.721–0.911)	2003-08-24	2006-09-05	−17.3 to −5.1	−17.3 to −5.1	47	60–200
ACS/HRC/F850LP	0.906 (0.844–0.985)	2006-07-25	2006-08-24	−3.5 to −4.6	−3.5 to −5.2	10	102
WFPC2/PC1/F450W	0.452 (0.404–0.504)	2007-05-20	2007-10-01	0.6 to −1.8	−2.2 to −0.7	15	160–200
WFPC2/PC1/F606W	0.579 (0.499–0.677)	2007-05-20	2007-10-01	0.6 to −1.8	−2.2 to −0.7	261	50–100
WFPC2/PC1/F814W	0.817 (0.725–0.936)	2007-05-20	2007-10-01	0.6 to −1.8	−2.2 to −0.7	16	200
WFPC2/PC1/F850LP	0.955 (0.875–1.051)	2007-07-28	2007-07-29	0.6	−1.5	6	140
WFC3/UVIS/F350LP	0.553 (0.412–0.788)	2011-10-13	2013-09-10	14.7–24.5	15.6–23.3	108	224–292
WFC3/UVIS/F475W	0.476 (0.421–0.536)	2010-10-13	–	10.5	11.5	2	170
WFC3/UVIS/F606W	0.579 (0.499–0.680)	2010-09-12	2010-11-30	11.7–9.3	11.2–12.1	56	268
WFC3/UVIS/F814W	0.790 (0.719–0.895)	2010-10-13	–	10.5	11.5	2	170
WFC3/UVIS/F845W	0.842 (0.809–0.880)	2009-10-13	2010-08-05	6.2–13.0	7.5–10.8	36	35

[a] Program ID's: Advanced Camera for Surveys (ACS)/HRC: 9823, 10102, 10473, 10534, 10805, 10870. Wide Field/Planetary Camera 2 (WFPC2)/PC1: 10870, 11118, 11292. WFC3/UVIS: 11630, 12245, 12665, 13055. [b] B and B_0 are the apparent ring opening angles (in degrees) as seen from Earth and the Sun. [c] N is the number of exposures.

$$\mathrm{NEW} = \int_{r_{\min}}^{r_{\max}} \mu \frac{I}{F}(r)\, dr. \tag{2}$$

Here, $I/F(r)$ is the reflectivity profile of the ring as a function of distance r from the center of Uranus. The factor μ equals $\sin(B)$, where B is the ring opening angle; for an optically thin ring, this factor accurately converts between the I/F in an image and the "normal I/F", which would have been obtained from a (hypothetical) view looking vertically downward through the ring plane (i.e., close to the views in Figure 4). The radial limits $r_{\min}$ and $r_{\max}$ refer to the radial boundaries of the ring in question. NEW is thus the radial width of a hypothetical ring with unit reflectivity ($I/F = 1$, i.e., a perfect Lambertian reflector) that reflects the same amount of light as the actual ring. This definition of NEW is ideal for our purposes, because it is independent of image resolution and viewing geometry.

For edge-on views of the rings such as were obtained by Keck and HST during RPX in 2007, we are not able to obtain the radial profile directly; instead, each pixel in an edge-on view samples an extended range of radii r, where r is the distance from the center of the planet as projected on the sky for a ring with radius x, as visualized in Figure 7. In this context, the most readily obtainable measurement is the vertical I/F (VIF), defined as

$$\mathrm{VIF}\,(r) = \int \frac{I}{F}(r,z)\, dz, \tag{3}$$

where z is the projected distance vertically from the edge-on ring plane. This represents a vertical integration across the edge-on rings, which is necessary in order to ensure that all ring's reflected light is included after it has been dispersed by the PSF of the telescope. This integration also accounts for the ring's true vertical thickness if it is nonzero.

VIF is related to the radial profile via the Abel Transform which, for optically thin rings, accounts for the way that each location in the edge-on profile samples a weighted integral across the ring plane as follows (Figure 7):

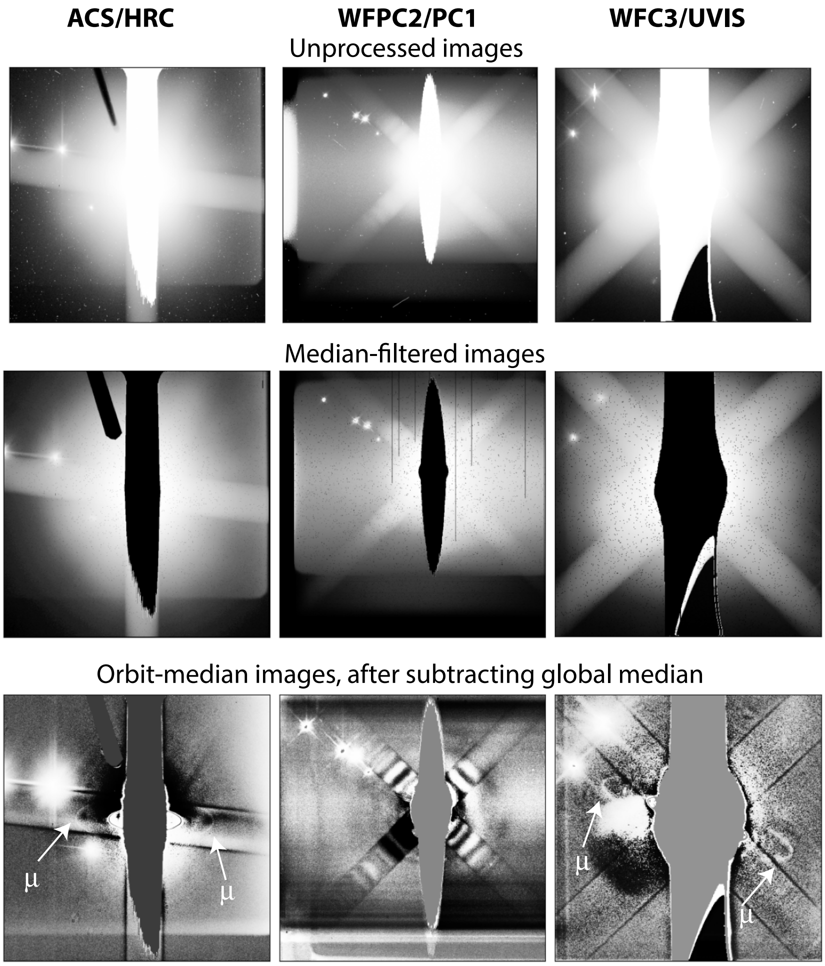

Figure 5. HST: Top row: Example un-processed images of the Uranus system from Hubble Space Telescope (HST). The three panels show images from Advanced Camera for Surveys (ACS)/High Resolution Channel (HRC) (j8oa02gxq_flt.fits), Wide Field/Planetary Camera 2 (WFPC2)/PC1 (u9ng5101m_c0m.fits), and WFC3/UVIS (ibqq31oxq_flt.fits), respectively. Each of these was taken through the instrument's broadest filter: CLEAR, F606W, and F350LP, respectively. Each image is presented using histogram equalization, which is necessary to show the details of the faintest portions of the image given the very large dynamic range. In each case, Uranus is near the center and intentionally overexposed, yielding vertical "bloom" of saturated pixels, as well as large, broad diffraction spikes. Without further processing, the rings are lost within this glare, although numerous moons are visible. Additional speckles in the image are the result of hot pixels and cosmic ray hits. Middle row: Median-filtered images from the top row. (left) The median of 8 CLEAR-filter ACS/HRC images from the first orbit of Visit 02 in program 9823, (j8oa02gxq_flt.fits–j8oa02h5q_flt.fits). (middle) The median of 12 F606W-filter WFPC2/PC1 images from the first orbit of Visit 51 in HST program 10870 (u9ng5101m_c0m.fits–u9ng510dm_c0m.fits). (right) The median of 10 F350LP-filter WFC3/UVIS images from Visit 31 of program 12665, and WFC3/UVIS (ibqq31oxq_flt.fits–ibqq31p6q_flt.fits). All images are shown using an equalized histogram. The prominent cosmic ray hits have been largely eliminated, as well as all but the brightest moons. Masked pixels, including those identified as hot or saturated, are all shown in black. Bottom row: Orbit-median images after subtracting the global median as discussed in Step 3 of Section 2.3 (see Figure 6).

$$\mathrm{VIF}\,(r) = 2\int_r^{\infty} \frac{I}{F}(x)\frac{x}{\sqrt{x^2 - r^2}}dx \tag{4}$$

If a ring is relatively narrow and we know its radial profile, we can define a relationship between VIF and NEW. For the μ and ν rings, we already know that the profiles are roughly triangular in shape (Showalter & Lissauer, 2006). In this investigation, we have refined the ring shapes further, as described in Sections 3.3 and 3.4 below. Figures 8 and 9 illustrate the relationship between NEW and VIF for shape models derived from the

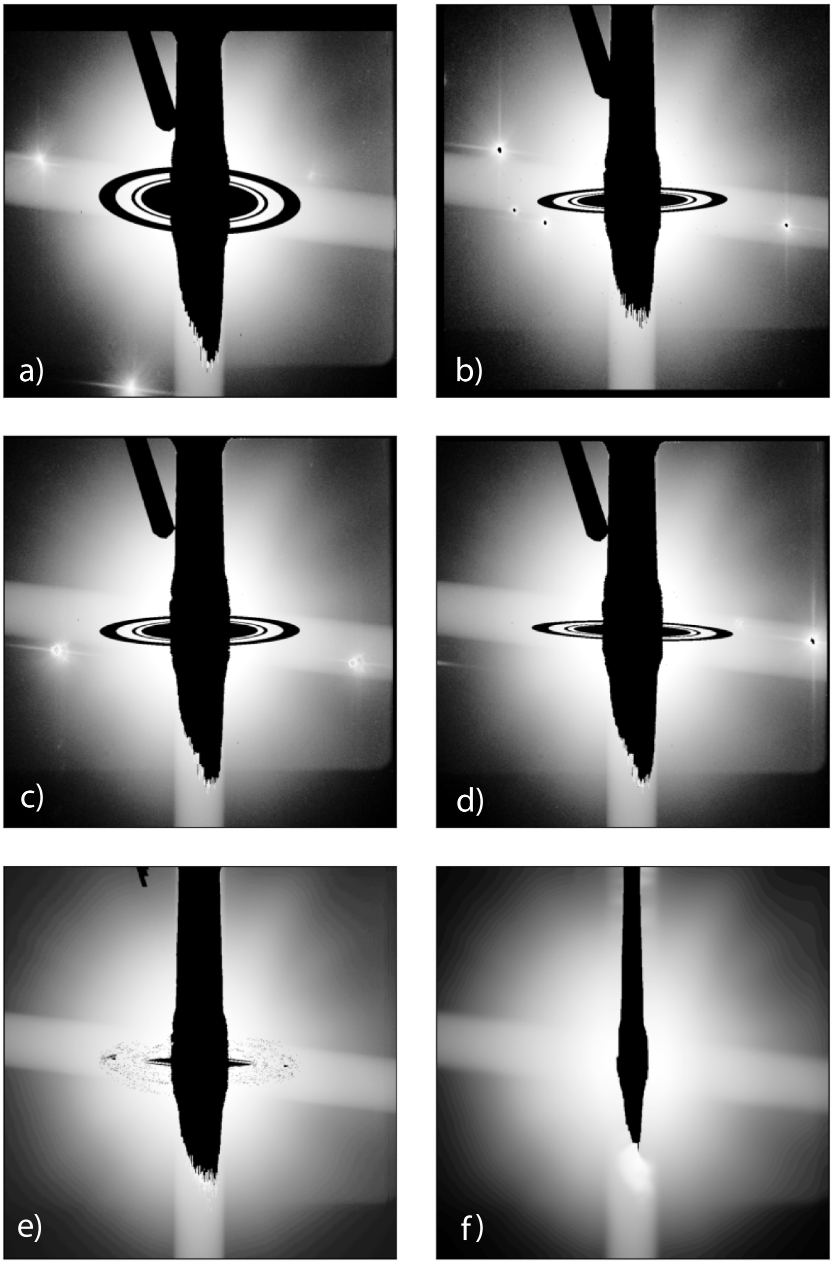

Figure 6. HST: An illustration of the steps involved in constructing a model glare image for a particular instrument and filter. Panels (a–d) CLEAR images from each year 2003–2006 in the ACS/HRC data. In each case, the pixels falling within the known radial boundaries of the outer rings are marked in black, as are all the pixels that were previously identified as masked. (e) A weighted median of all the available images, masked in this same manner. Some black speckles remain, and two small black triangular areas near the μ ring ansa indicate pixels that were never sampled without the presence of a ring. However, these can be smoothed away via a gaussian filter, as is shown in panel (f). These are the final background images we have subtracted from the individual frames, as illustrated in the bottom row of Figure 5.

NIRCam data (Section 3.3); the former shows simple models that match the data, and the latter shows how these models are expected to appear in edge-on views for optically thin rings.

We discuss the results obtained from each telescope in the next three subsections.

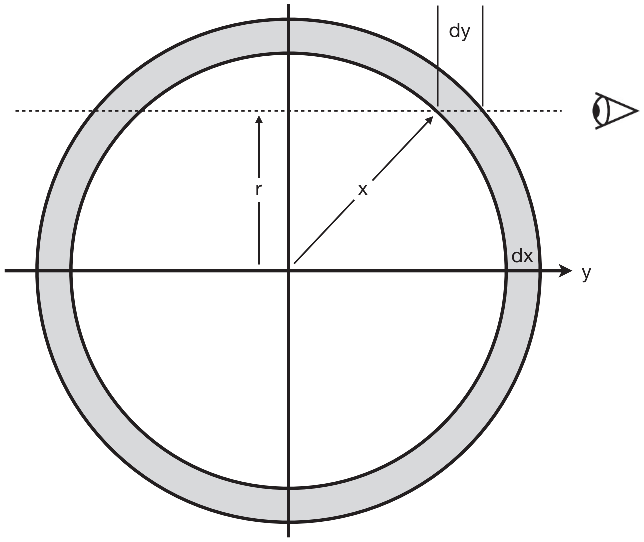

Figure 7. An illustration of the Abel Transform. It shows a narrow ringlet of radius x and width dx, supposing it is viewed edge-on from the right. At a projected distance r from the planet center, the contribution of this ringlet to the observed intensity is enhanced by a factor $2\ dy/dx$. Equation 4 accounts for this overall enhancement.

3.2. Results From the Keck Observations

Figure 10 shows scans through the Keck images along the ring plane. Along the left axis, the axis indicates the sum of I/F over the 30 rows of pixels centered on the ring plane; along the right, this is converted to vertically integrated I/F, or VIF (Equation 3), referred to below as VIF_μ and VIF_ν for the two rings.

To construct high SNR scans through the μ and ν rings, perpendicular to the ring plane, we averaged rows on the images in Figure 2 over the brightest section of each profile, corresponding to a distance 73,500–98,500 km for the μ ring and 60,740–67,740 km for the ν ring. Results for the two rings on the different days and wavelengths are shown in Figure 11. The H-band data have a particularly high background signal because, at the time, Uranus's pole was brighter at the South than North pole, contributing scattered light that was quite asymmetric with respect to the ring plane. We modeled the background with a polynomial (order 2, 3, or 4); the red curves in Figure 11 show the inner part of the polynomials (i.e., the fits were obtained over the full ~55,000 km across the images, rather than the ~30,000 km shown on the plots). These polynomials were subtracted from the scans. The results are shown in the right columns for each ring.

We determined the VIF for each ring (Equation 3) from the scans in Figure 11. The results are shown in Table 4. The uncertainties on the VIFs were determined from the standard deviation in the scans away from the rings, multiplied by $\sqrt{N}$, with N the number of data points used in the summation over the rings. We added an extra 10% of the measured VIF in quadrature due to estimated uncertainties in the background subtraction (note that this 10% dominates the error).

We note that when observing a point source with AO, some light is scattered into the halo of the point spread function (PSF). Hence, the flux density as measured may be too low unless one corrects for this effect through comparison with a bright star, as explained in detail by Gibbard et al. (2005) and de Pater et al. (2014). Usually the integration limits in Equation 3 are larger than the extent of the PSF, except for the August μ ring data, where the integration limits are smaller. In this case the measured VIF_μ was increased by a factor of 1.15 to correct for the loss of flux into the wings of the PSF.

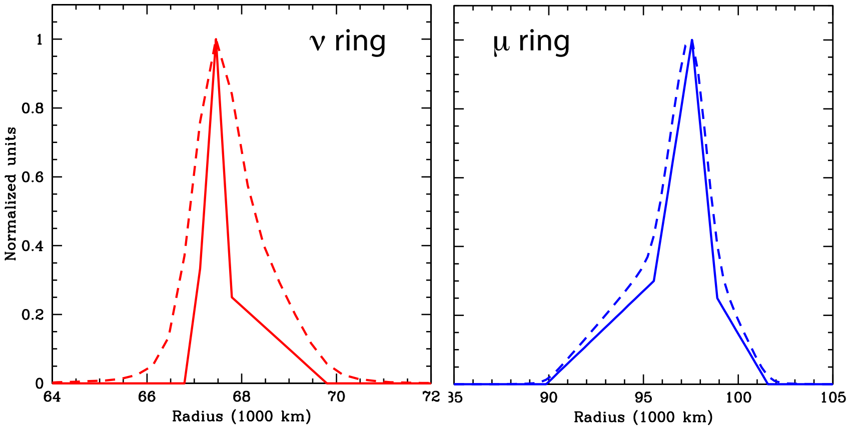

Figure 8. Adopted, piecewise linear models of the ν and μ rings that were used to derive the normal equivalent width in each of the James Webb Space Telescope filters (Table 5). These models are rough fits to the F150W2 data. The dashed lines show the models after convolution with the F150W2 point spread function (PSF). Each profile is normalized to unity. Note the very narrow ν ring profile before convolution with the PSF. For the μ ring, r_{min}, r_{peak}, and r_{max} are 89,866, 97,558, and 10,1572 km, resp. For the ν ring they are: 66,789, 67,458, and 69,799 km, resp.

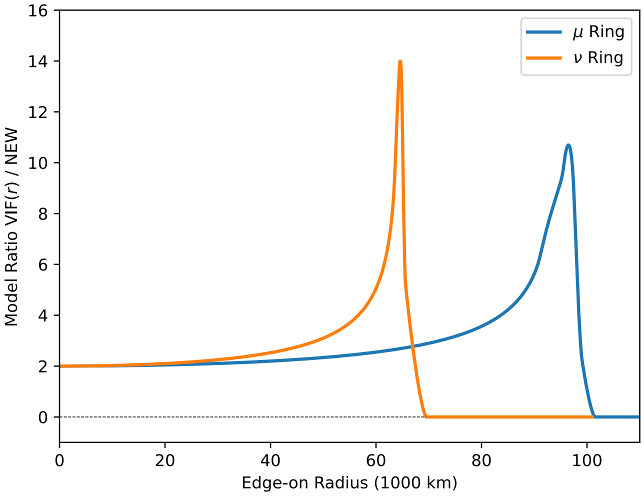

Figure 9. The models of Figure 8 converted to edge-on views using Equation 4. The vertical axis is the enhancement factor relative to the normal equivalent width.

In addition to a direct integral of VIF from the data, we used an alternative approach involving the ring model. The observations, and hence scans, show the rings convolved with the PSF. We constructed a PSF from stellar images in K′ band (Figure 7 in de Pater et al. (2013)). We then made 1-dimensional (1D) models of the rings (red profiles in Figure 11), convolved these with the 1D PSF (blue profiles), and compared these models with the observations in Figure 11. For the H band data we used a scan through Miranda, which traveled "through the image" adjacent to the main rings; since its orbit is slightly inclined, the moon was visible next to the main rings, and did not affect the outer rings themselves. The Miranda H band scan was essentially the same as the stellar K′ band PSF. The VIFs based upon these models agree very well with the data (Table 4).

We follow the procedure outlined in Section 3.1 to convert from VIF to NEW. Within the radial limits derived above (Figure 8), the ratio VIF/NEW is 5.2 for the μ ring and 7.5 for the ν ring. These numbers change only slightly if the radial extent from Showalter and Lissauer (2006) is used (5.1 and 7.6 for the μ and ν rings, resp.). These factors do not take into account the superposition of the ν and μ rings when evaluating the ν ring. If the rings are optically thin and radiation along the entire line-of-sight is received, we would need to subtract the contribution from the μ ring to get a measurement of just the ν ring. With the same numerical model used to relate the VIF to the NEW, we calculate that the VIF of the μ ring traversed over r = 60,740–67,740 km is a factor of 2 smaller than what we measured for the μ ring at r = 73,500–93,500 km. Hence, assuming the rings are optically thin, we need to subtract 0.5× the measured VIF_μ from the VIF_ν to get a proper measurement for the ν ring. The results for the VIF and NEW are summarized in Table 4.

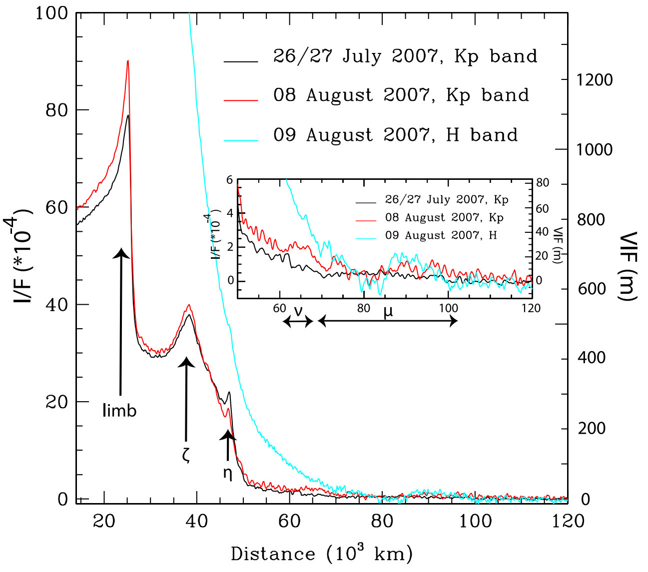

Figure 10. Keck: Scans along the ring plane, summed over 30 pixels centered on the rings. The y-axis shows the summed I/F on the left and converted to VIF in meters on the right (a pixel scale of 139.1 km/pixel [Table 1] was used to convert I/F into VIF). The x-axis is the projected radial distance from the center of the planet. The inset shows an enlargement of the μ and ν rings, (boxcar) smoothed over 5 pixels radially. The limb, ζ and η rings are indicated, as well as the approximate extent of the μ and ν rings on the inset.

3.3. Results From the JWST/NIRCam Images

To obtain radial scans through the JWST/NIRCam data, we first reprojected the images in Figure 4 to generate the radius-vs-longitude maps in Figure 12. Both the μ and ν rings are visible in some of the maps, as might be expected based upon Figure 4. By averaging the data over longitude, we can increase the SNR. Column 1 in Figure 15 shows radial profiles between 40,000 and 130,000 km after the data had been averaged over longitude. These data show the original units (MJy/sr), and indeed the SNR is extremely high. Unfortunately, scattered light from Uranus and its rings is very high too. To better show the two outer rings, we made a 6th-order polynomial fit to the profiles, and subtracted this from the data; the results are shown in Column 2 of Figure 15. The units on these graphs are converted to NEW Equation 2. The rings are clearly visible in all filters, except in F070W, which is dominated by Uranus's scattered light. In most filters one can discern a dip in the intensity just interior to the ν ring (at ~60–65,000 km), and an increase at ~75,000 km. Both features are caused by the fact that the ν ring is superposed on the PSF of the bright ϵ ring, which has some slight 'kinks' or 'shoulders' in its profile. This is causing the dips and bumps interior and exterior of the ν ring.

In order to estimate and subtract the background more accurately, we constructed a longitudinal profile by median-combining 11 rows in Figure 12 on either side of the μ ring and 7 rows on either side of the ν ring. We then averaged the two median-combined profiles around each of the rings to create a background profile centered on each of the μ and ν rings. We then adapted the intensity level of these background profiles across 100 rows centered on the μ ring, and 40 rows on the ν ring by using the exponential fit discussed above. The results are shown in Figures 13 and 14 for the 2023/2024 and 2025

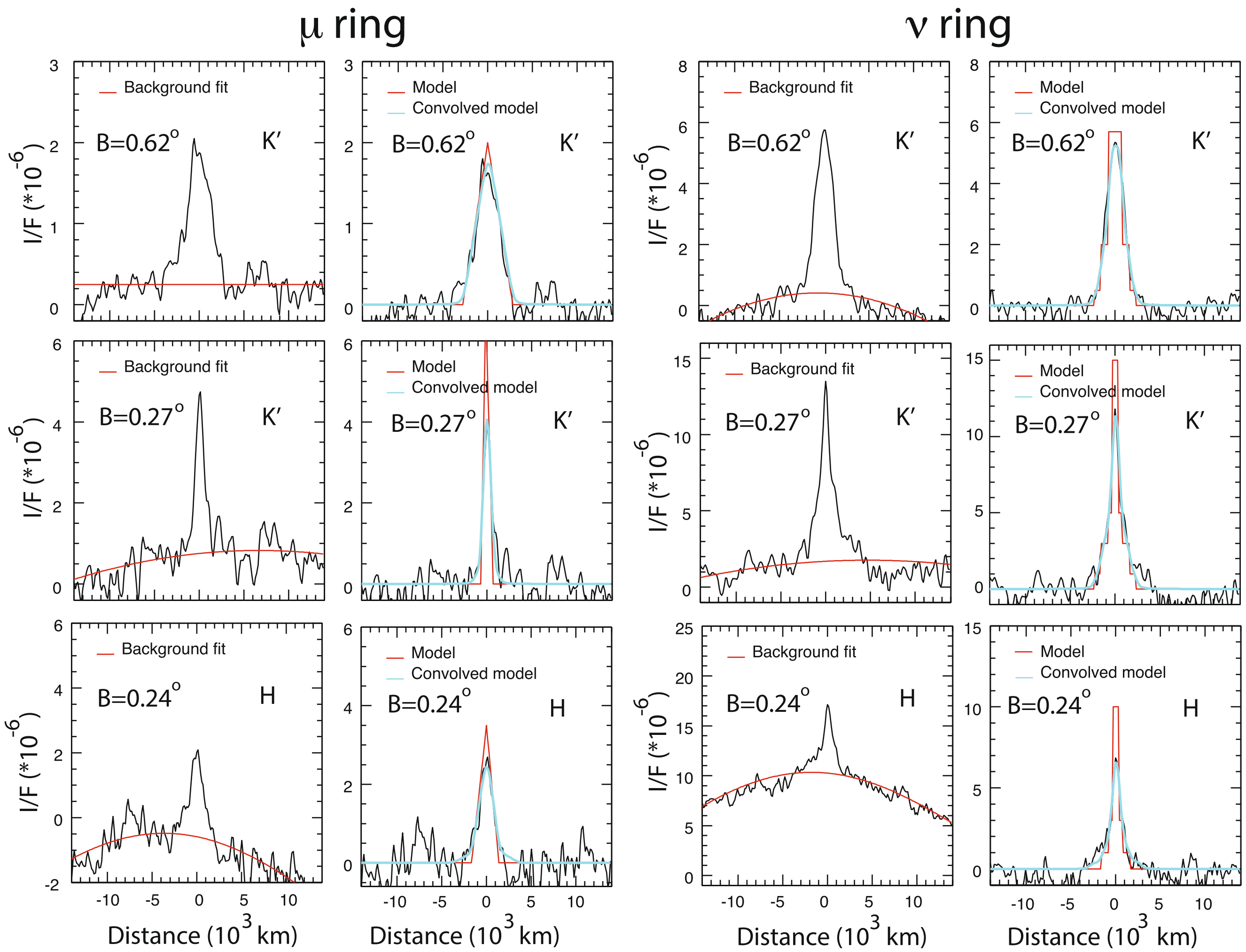

Figure 11. Keck: Vertical scans through the μ (left side) and ν (right side) rings, perpendicular to the ring plane. The top panels show the K′-band July 26/27 data; middle panels the K′-band August 8 data; the bottom panels the H-band data from August 9. The scans are averaged over a projected radius 73,500–98,500 km for the μ ring and 60,740–67,740 km for the ν ring. The left columns for each ring show the original data together with a fit to the background; the right columns show the scans after subtracting this background. An offset of 2×10^{-7} in I/F was added to the H band data for the ν ring to bring the background closer to zero. Fits (by eye) are superposed, where the red profile is the ring profile (model), which after convolution with the point spread function (blue profile) gave a good fit to the data. Note that the scans through the ν ring are contaminated by the μ ring in this almost edge-on geometry. We correct for this contamination when converting from VIF to normal equivalent width, as explained in Section 3.1.

Table 4
Keck/NIRC2: Measured Parameters for the μ and ν Rings of Uranus

Date (UT) 2007	Band	B (deg)	VIF$_{\mu}^{a}$ Data (m)	VIF$_{\nu}^{a}$ Data (m)	VIF$_{\mu}^{b}$ Model (m)	VIF$_{\nu}^{b}$ Model (m)	NEW$_{\mu}^{c}$ Data (m)	NEW$_{\nu}^{c}$ Data (m)	NEW$_{\nu}^{d}$ Data (m)
July 26	K′	0.62	5.4 ± 0.6	13.0 ± 1.3	5.6	12.8	1.04 ± 0.12	1.7 ± 0.2	1.2 ± 0.14
July 27	K′	0.60	5.4 ± 0.6	13.0 ± 1.3	5.6	12.8	1.04 ± 0.12	1.7 ± 0.2	1.2 ± 0.14
August 08	K′	0.27	5.7 ± 0.5	19.4 ± 2.5	4.8	21	1.10 ± 0.12	2.6 ± 0.3	2.0 ± 0.3
August 09	H	0.24	4.8 ± 0.5	10.5 ± 1.1	5.3	11.1	0.93 ± 0.12	1.4 ± 0.15	0.9 ± 0.14

Note: Note that the VIF values are for the "front + back" side of the rings, and the ν ring is affected by the μ ring. The NEW values are determined from the VIF values by applying a model of uniform optically thin rings, as explained in the text. [a]VIF: Vertically integrated I/F of the μ and ν rings. July 26 and 27 were averaged, so the same values are shown. [b]VIF: Vertically integrated I/F of the μ and ν rings derived by fitting rings to the data. July 26 and 27 were averaged. [c]NEW: normal equivalent width, that is, the EW of the rings when seen "face-on". [d]NEW$_{\nu}$ after subtracting the μ ring (see text).

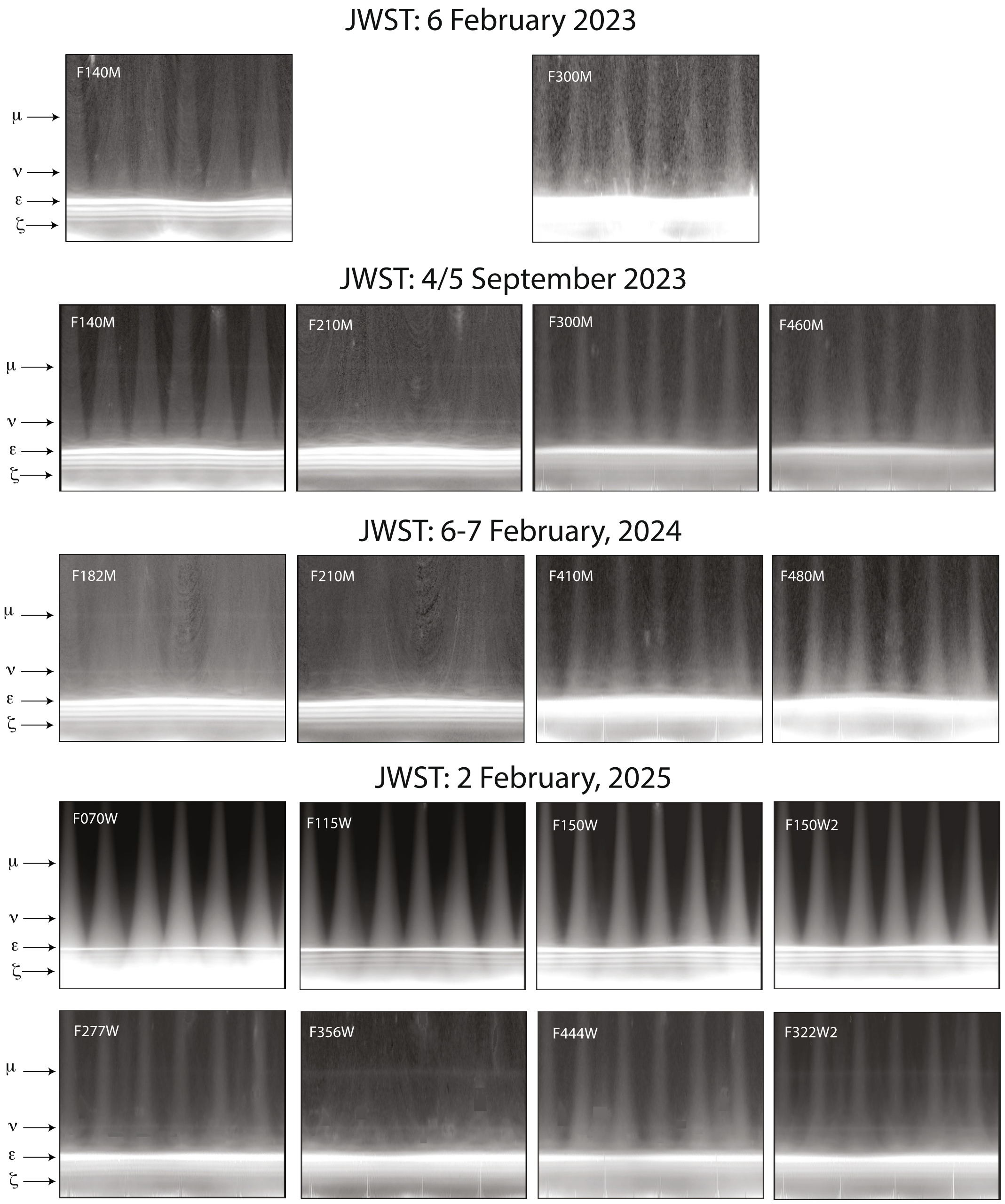

Figure 12. JWST/NIRCam data from Figure 4 reprojected, with radius along the y-axis from 30,000 to 130,000 km, and a full 360° in longitude along the x-axis. The μ, ν, ϵ, and ζ rings are indicated; note the "waviness" of the ϵ ring, caused by the eccentricity of this ring. In between the ζ and ϵ rings one can discern 3 clusters of rings: the rings 6, 5, 4 closest to the ζ ring, next the α, β rings, and closest to the ϵ ring the η, δ, γ rings. The data are displayed with IDL's ATV, with the asinh scaling (as in Figure 1) to bring out the various features.

data, respectively. In the first figure, the μ ring is extremely faint in the F300M and F410M filters, and essentially invisible in F460M and F480M. The ν ring is perhaps faintly visible in the latter two filters, but because the radial profiles are very noisy and much broader than expected as shown below, we do not trust these data. In 2025, neither of the rings is visible in the F070W filter. In all other filters the rings show up very clearly, albeit a bit faint in F444W. We further note that the μ ring appears to be slightly wavy in the F150W and F150W2 filters, that is, it does not precisely follow a straight line as one would have expected for a circular ring. This is addressed in Section 4.3.

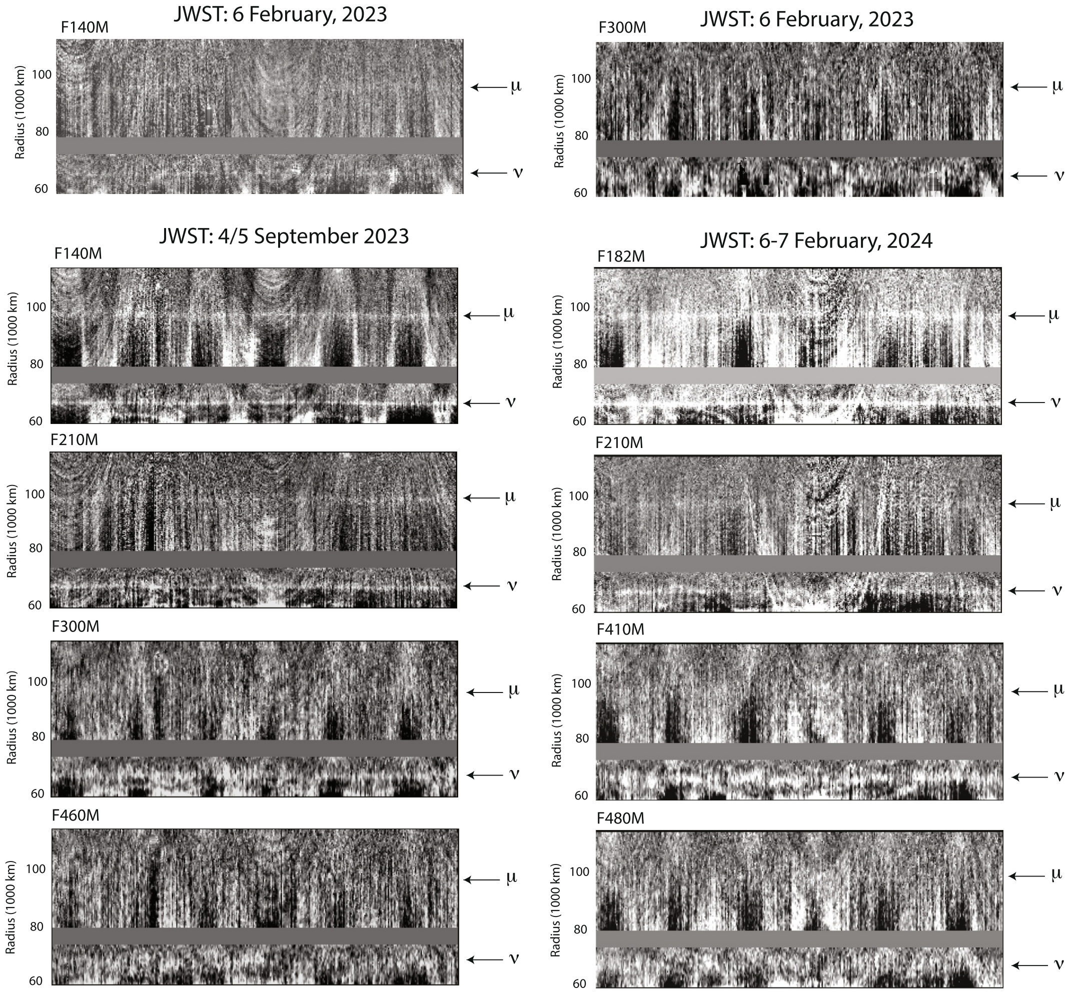

Figure 13. JWST/NIRCam: Reprojected maps of the μ and ν rings from 2023 February 6 in the top row (program #2739), 2023 September 4/5 on the left side in rows 2–5 (program #2739), and from 2024 February 6–7 on the right side in rows 2–5 (program #2768). These maps were derived from Figure 12, after fitting and subtracting background profiles from Figure 12 as discussed in the text. The images are shown on a linear scale, with a full 360° in longitude along the x-axis.

After averaging over longitude (skipping contaminated regions) and adjusting the background level using a polynomial fit of order 1–6 (the order that best fits the background is chosen for each filter), we produce the scans through each of the rings as shown in Columns 3 and 4 of Figure 15. The ν ring profiles in the F460M and F480M filters are very noisy (large fluctuations in I/F around the ν ring in Column 2 of Figure 15) and unrealistically broad (in Column 3 of Figure 15). So even though this ring may be faintly visible in Figure 12, we do not trust these data.

We integrated the normal I/F over the extent of the μ (88,500–102,000 km) and ν (66,000–71,000 km) rings in Figure 15 to determine the normal equivalent width, NEW. The results are summarized in Table 5. The uncertainties are based on the root-mean-square variations in the scans outside the rings.

Because we need to determine the NEW for many filters, including those where the SNR is relatively poor, we also used an alternative technique based on the assumption that the rings' radial profiles are the same, except for an overall scaling factor, at all JWST wavelengths. We described each ring using a simplified model consisting of 3–4 linear segments, as was illustrated in Figure 8. The models were derived via manual fits to the F150W2 data from February 2025, but provide an accurate match to all ring profiles between 1.4 and 2.1 μm; outside this range of wavelengths, ring profiles are too noisy to assess the models' accuracy. Using linear least-squares, we then determined the best-fit scale factor required to minimize the residual between the model (after convolution with the PSF) and each scan, after removal of the background polynomial. Because this procedure enforces a particular

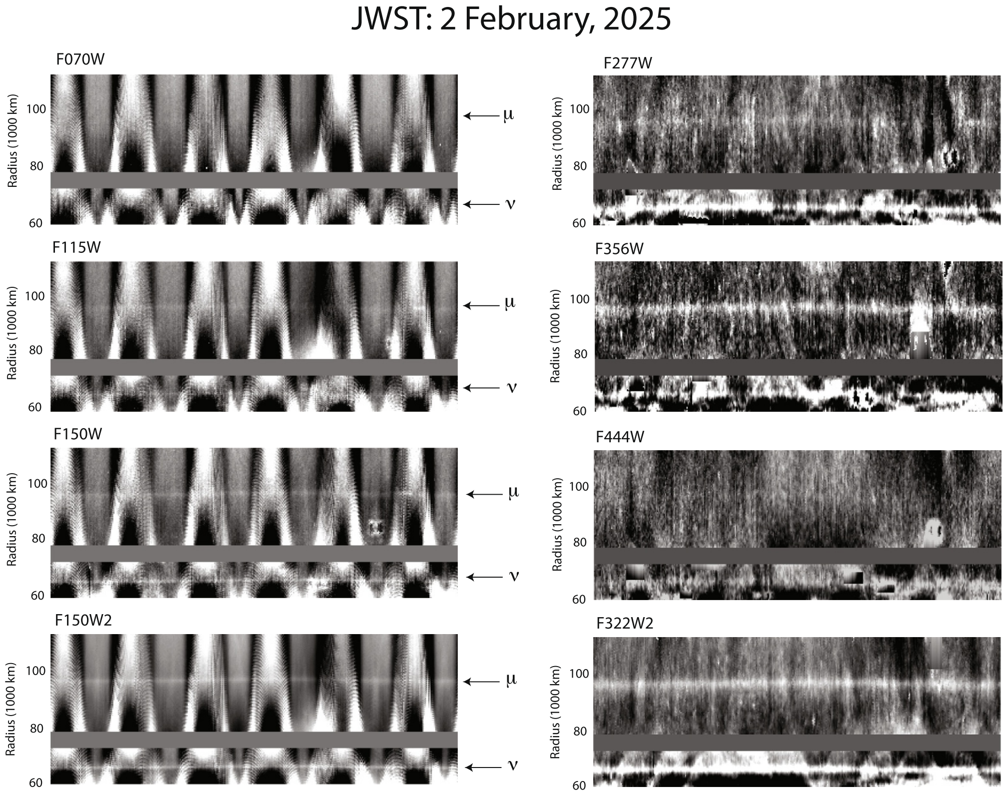

Figure 14. JWST/NIRCam: The μ and ν rings from #6379, reprojected after background profiles derived from Figure 12 were subtracted from Figure 12, as discussed in the text. The data from the short-wavelength filters are shown on the left; the long-wavelength filters on the right. The two broadband filters are shown in the bottom row. These images are shown on a linear scale, with a full 360° in longitude along the x-axis. Note that in particular the μ ring is not straight, possibly indicative of a slight eccentricity (see Section 4.3).

shape for the ring profile, it is better able to obtain consistent results from the noisiest profiles. The resulting models are superposed as dotted lines on the data in Figure 15.

We initially downloaded the model PSF for each filter from the Space Telescope Science Institute. However, because the PSF peak was spread over 2 pixels in these simulated PSFs, rather than 1 pixel, a better PSF was constructed from images of Miranda in individual dithers of the #2739 and #2768 programs. These PSFs were adjusted to the same scale as our ring scans (334.448 km/pixel) using the congrid function in IDL, and averaged over azimuth. Images of the PSF as well as scans at several wavelengths are shown in the Appendix, Figures A1 and A2. PSFs in filters where we did not have images of Miranda were interpolated such that the PSFs' Full Width at Half Power scaled roughly linearly with wavelength. The NEW values determined from this approach are tabulated in the "model" columns of Table 5. Uncertainties are derived from the χ^2-fit ($\sqrt{\chi^2/N}$), indicating the goodness of the fit. Overall, these values agree quite well with those obtained by direct integration.

3.4. Results From the HST Data

HST observations of Uranus tend to center around its opposition, which fell between late August and early October during 2003–2013. For this reason, we grouped our data by calendar year in this analysis. For the years before and after the 2007 RPX, we converted our glare-subtracted images to radial profiles and then obtained the NEW as follows:

1. We defined a new pixel mask to block out any remaining flaws in the orbit-combined images. These were caused by background stars, incompletely masked moons, or residual glare patterns.
2. We defined the longitude limits of a "wedge" of pixels surrounding each ring ansa, where the radial resolution is finest. This wedge typically spanned 80° of longitude, but smaller in 2006 when the rings were less open.

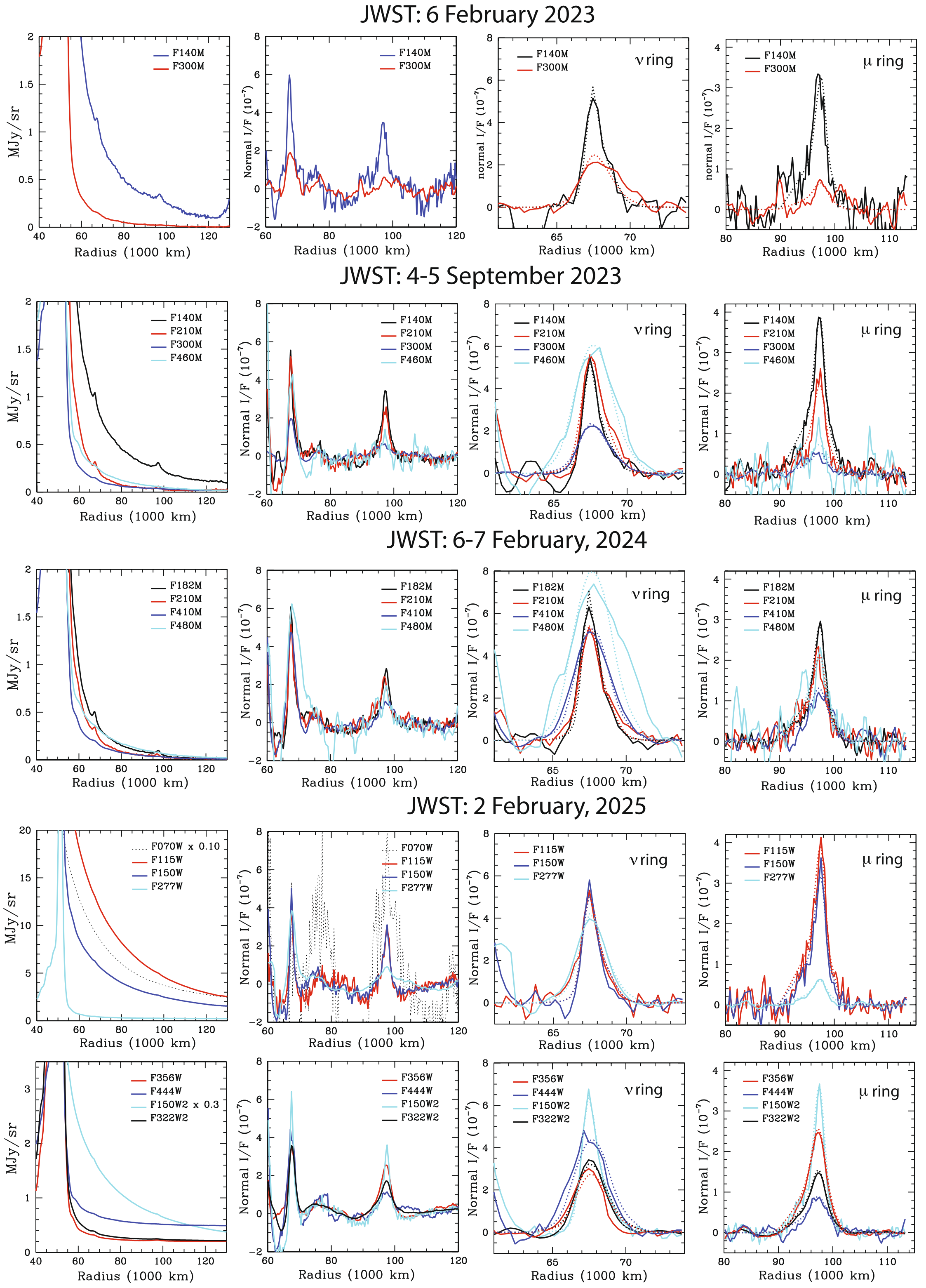

Figure 15. JWST/NIRCam: Column 1: Scans through the rings in Figure 12 after averaging over longitude (x-axis in Figure 12). Column 2: Scans after subtraction of a polynomial fit to the scans in Column 1. Columns 3 and 4: Final scans through the ν and μ rings, resp., with best-fit models (dotted lines) superposed.

Table 5
JWST/NIRCam: Measured Parameters for the μ and ν Rings of Uranus

Date (UT)	Filter	NEW$_\mu$ Data (m)[a]	NEW$_\mu$ Model (m)[b]	NEW$_\nu$ Data (m)[a]	NEW$_\nu$ Model (m)[b]
2023, February 6	F140M	1.27 ± 0.17	1.23 ± 0.02 (0.03)	0.90 ± 0.12	0.89 ± 0.011 (0.021)
2023, February 6	F300M	0.43 ± 0.06	0.30 ± 0.01 (0.01)	0.72 ± 0.04	0.66 ± 0.012 (0.018)
2023, September 4	F140M	1.47 ± 0.06	1.57 ± 0.01 (0.03)	0.80 ± 0.03	0.84 ± 0.011 (0.02)
2023, September 4–5	F210M	0.76 ± 0.05	0.94 ± 0.01 (0.02)	1.07 ± 0.04	1.10 ± 0.014 (0.03)
2023, September 4	F300M	0.25 ± 0.02	0.26 ± 0.01 (0.01)	0.59 ± 0.02	0.62 ± 0.003 (0.01)
2023, September 4–5	F460M	0.28 ± 0.08	0.39 ± 0.01 (0.02)	1.92 ± 0.09	1.98 ± 0.013 (0.04)
2024, February 6–7	F182M	1.09 ± 0.05	1.16 ± 0.01 (0.02)	1.13 ± 0.04	1.10 ± 0.02 (0.03)
2024, February 6–7	F210M	0.88 ± 0.05	0.91 ± 0.01 (0.02)	1.14 ± 0.05	1.07 ± 0.01 (0.02)
2024, February 6–7	F410M	0.58 ± 0.04	0.66 ± 0.01 (0.02)	1.55 ± 0.04	1.56 ± 0.01 (0.04)
2024, February 6–7	F480M	1.13 ± 0.09	1.09 ± 0.02 (0.03)	2.84 ± 0.08	2.71 ± 0.04 (0.07)
2025, February 2	F115W	1.42 ± 0.06	1.59 ± 0.009 (0.03)	1.0 ± 0.04	0.84 ± 0.02 (0.03)
2025, February 2	F150W	1.09 ± 0.05	1.28 ± 0.006 (0.03)	0.68 ± 0.03	0.84 ± 0.02 (0.03)
2025, February 2	F150W2	1.22 ± 0.05	1.34 ± 0.006 (0.03)	1.05 ± 0.03	1.06 ± 0.01 (0.02)
2025, February 2	F277W	0.23 ± 0.04	0.28 ± 0.014 (0.02)	1.00 ± 0.03	1.03 ± 0.01 (0.02)
2025, February 2	F322W2	0.69 ± 0.03	0.76 ± 0.002 (0.03)	0.81 ± 0.02	0.90 ± 0.01 (0.04)
2025, February 2	F356W	1.13 ± 0.04	1.28 ± 0.003 (0.03)	0.69 ± 0.03	0.78 ± 0.02 (0.03)
2025, February 2	F444W	0.35 ± 0.04	0.46 ± 0.003 (0.01)	1.28 ± 0.03	1.38 ± 0.02 (0.03)

[a] The error is derived from the standard deviation away from the line profiles, and the absolute calibration in quadrature. [b] The error is the uncertainty on the model fit, while the error in brackets includes the error on the absolute calibration in quadrature. Absolute calibration: we used a conservative 2% for all filters, and 4% for F322W2 and F460M. https://jwst-docs.stsci.edu/jwst-calibration-status/nircam-calibration-status/nircam-imaging-calibration-status#NIRCamImagingCalibrationStatus-Photometriccalibration.

3. We defined radial bins in steps of 500 km for the μ ring and 250 km for the ν ring. We converted images to radial profiles by obtaining the mean normal I/F among the pixels that fell within each bin. Figure 16 shows some of these profiles.
4. Although the μ ring is apparent in many of the profiles, these profiles contain large radial gradients, which are caused by the residual glare pattern in the images (Figure 5, bottom row). To measure the radially integrated μ ring, we took advantage of the fact that it has a known, roughly triangular radial profile (Figure 8). We modeled each profile as a low-order polynomial in r plus an amplitude factor times the ring's radial model (Figure 16). The complete model for a ring profile is:

$$p(r) = a\, m(r) + \sum_{i=0}^{N} c_i\, b_i(r), \tag{5}$$

where $m(r)$ is the ring model, $b_i(r) = r^i$ are the polynomial terms describing the background, a and c_i are the coefficients, and N is the order of the background polynomial. We used linear least-squares methods to obtain the best-fit values for the coefficients along with their variances and covariances.

5. The value we seek is the integral of the ring model after subtracting off the background. Let M and B_i represent the integrals of $m(r)$ and $b_i(r)$ between the ring's radial limits. Straightforwardly, the best-fit value of NEW is aM. The uncertainty, however, involves all of the coefficients:

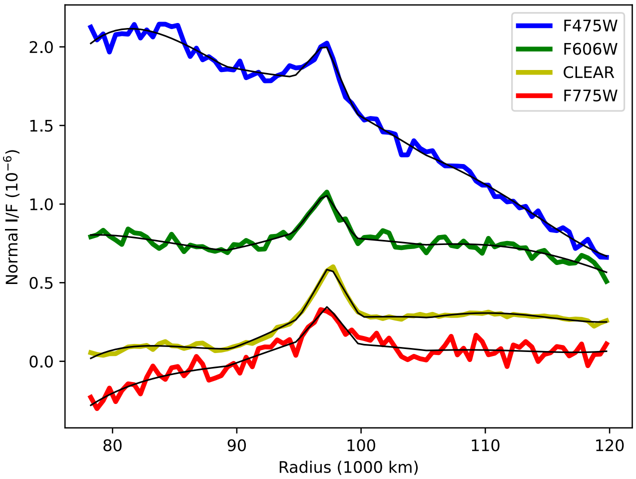

Figure 16. HST/ACS: Profiles of the μ ring from four ACS/HRC filters. For each profile, a thin black line shows the fitted model, involving a low-order background polynomial plus an amplitude factor times the ring model. The variations of each profile outside the ring limits provide a visual indication of the noise level.

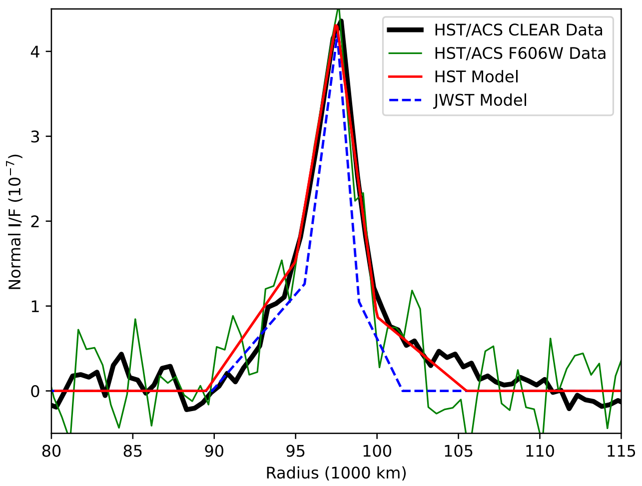

Figure 17. HST: The μ ring's radial profiles compared to two different piecewise-linear models. The profiles are from our two highest-SNR, finest-resolution image sets, ACS CLEAR and F606W. The red line has been manually aligned to the data, whereas the blue line is the one derived for the James Webb Space Telescope data (see Figure 8). The red line provides a much better fit to the HST data and was used for all HST data analysis.

$$d(\mathrm{NEW})^2 = \sigma^2 \left[\mathrm{var}(a) M^2 + \sum_i \mathrm{var}(c_i)\, B_i^2 - 2\sum_i \mathrm{cov}(a, c_i)\, M B_i - 2\sum_i \sum_{j \neq i} \mathrm{cov}(c_i, c_j)\, B_i B_j \right], \qquad (6)$$

where σ is the root-mean-square residual between the overall model $p(r)$ and the measured profile.

Upon implementing Step 4, however, it became apparent that the μ ring's radial profile is wider in the HST data than in the JWST data. Figure 17 compares radial profiles derived from the HST data with the JWST model (Figure 8) and with an alternative model that provides a far more accurate fit to the HST data. This is a manual fit to the profiles, designed to accommodate the common traits among the HST profiles as well as the uncertainties in its radial limits. The comparison reveals that the radial width of the ring is wavelength-dependent. Most notably, the ring has an outward extension in these profiles, which have a mean wavelength of 0.6 μm; this is discussed further below (Section 4.3). The plots in Figure 16 actually use this broader model. Table 6 summarizes our measurements of the μ ring obtained using this procedure.

The ν ring is too narrow to detect clearly in the WFC3/UVIS instrument; our only clear detections are from the ACS/HRC. Furthermore, it is too narrow to use the model-fitting approach. Instead, we model the background using a low-order polynomial fitted to the regions of the profile outside the ring's radial limits and subtract; the NEW is the remaining area under the curve after the subtraction. Because we cannot be certain of the "best" background model, we fitted a large number alternative second- and third-order polynomials and allowed the standard deviation among the NEW determinations to define the estimated uncertainty (Figure 18). Inner limits of the fits ranged from 62,250 to 65,000 km and outer limits from 71,250 to 74,000 km; in all cases, the radial limits of the ring, between 66,000 and 70,000 km, were excluded.

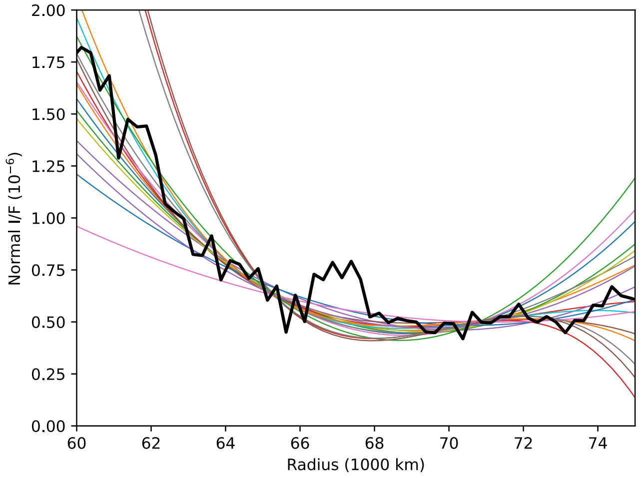

Figure 18. HST: An illustration of our procedure for measuring the normal equivalent width of the ν ring. Its radial profile from the F606W filter of the ACS/HRC is shown as a heavy black line. For comparison, we show a large number of polynomial models, which have been fitted to the profile adjacent to the ring. We have used a variety of assumptions about the polynomial's order (2 or 3) and the fit's inner and outer radial limits. The area between the profile and each curve defines an estimate of NEW; the standard deviation among these values defines our inferred uncertainty.

We had to modify this procedure for the 2007 RPX data set, which was obtained with WFPC2. In this data set, the rings appeared edge-on, so we followed a procedure similar to that described in Section 3.2 for the Keck data. We started with the set of images of the type illustrated in the middle panel of Figure 5, which had been grouped by visit and filter, median-combined, and then had the global median glare pattern subtracted. Next, we rotated and resampled each image into a uniform square 200 × 200 km grid in (r, z) coordinates, where r is the projected distance from the Uranian pole and z is the distance above the ring plane. At this point, the geometry of every image was effectively identical. To further suppress the residual glare, we processed each column (along fixed r) in each the image by fitting a polynomial to the pixels above and below the ring plane (excluding the central ±2000 km, which contains the ring) and subtracted it. We could then median-combine images taken through the same filter into one image. Figure 19 illustrates these steps.

We then constructed vertical profiles of I/F within the radial limits 74,900–99,100 km, where the μ ring is brightest. These profiles still show modest background variations due to the incompletely subtracted glare. Assuming these variations are smooth, we fitted the profiles outside the ring plane to a variety of polynomials (Figure 20), subtracted, and then derived the VIF from the area under the curve that remained. We estimated the uncertainty as the standard deviation among the VIF values associated with the different background curves. Based on our model for the μ ring (Section 3.1), the ratio

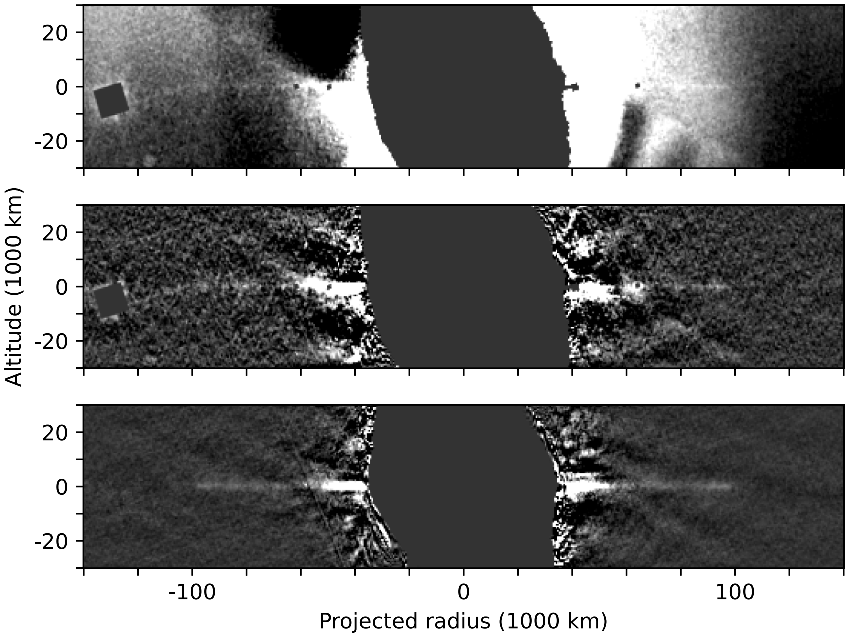

Figure 19. HST/WFPC2: Processing steps for the Wide Field/Planetary Camera 2 (WFPC2) images obtained during the 2007 RPX. Top: A median-combined image from visit 73, orbit 2, using the F606W filter. Middle: The same image after subtracting polynomial fits to the pixels above and below the ring plane. Bottom: The combined image from all WFPC2 F606W filter images.

of VIF/NEW within the radial limits is expected to be 5.2. Hence, as a final step, we divided by 5.2 to obtain the NEW (Table 6). For the ν ring, we applied the same technique to vertical profiles between the radial limits 65,000–68,000 km, and then subtracted out the μ ring's expected contribution. Although the ν ring was detected unambiguously, the measurement uncertainties are quite large.

Edge-on measurements of the ν ring were still more challenging because we also had to subtract off the (highly uncertain) overlapping contribution of the μ ring. We derived vertical profiles between radial limits 65,000–68,000 km and followed the same procedure as above to estimate VIF and its uncertainty. We expect VIF/NEW = 11.1 for the ν ring, but also VIF/NEW = 2.8 for the μ ring (these numbers differ some from those in Section 3.2 due to different integration limits—See Figure 9). We therefore take the μ ring's inferred NEW values, scale them to VIF within these radial limits, and subtract them before converting the remainder to NEW for the ν ring. We combine the uncertainty in the μ ring's contribution in quadrature with that of the measured VIF to determine the accuracy of our ν ring measurement. The results are tabulated in Table 6.

To examine the μ ring values in more detail, we show NEW as a function of year for the two broadest HST filters, CLEAR from ACS/HRC, F606W from WFPC2, and F350LP from WFC3/UVIS (Figure 21). Error bars represent ± one standard deviation and are especially small during 2003–2006, when we obtained many very long integrations. During these years, NEW decreased in a roughly linear trend by more than a factor of two. This provides strong evidence that the ring is variable in brightness over time scales of a few years. Although the brightness shows a large upward jump in 2007, this measurement is unique in two regards—as our only measurement from WFPC2 and our only edge-on measurement from HST. We therefore prefer to be cautious about taking this measurement literally relative to the others. Unfortunately, the WFC3/UVIS measurements in later years never again achieved precision comparable to 2003–2006; thus, we cannot say whether the initial trend was purely temporary.

4. Discussion

4.1. Spectra

We combined the NEW values at all wavelengths from the three telescopes in Figure 22. As discussed in Section 3.3, we do not trust the NEW_μ and NEW_ν values at 4.6 and 4.8 μm, even though the ring scans, averaged over

Table 6
HST: Measured Parameters for the μ Ring of Uranus

Instr/Filter	Year	NEW_μ Fixed model with data (m)	NEW_ν Fixed model with data (m)
ACS/CLEAR	2003–2006	2.02 ± 0.29	0.40 ± 0.13
ACS/CLEAR	2003	2.56 ± 0.54	0.67 ± 0.23
ACS/CLEAR	2004	2.08 ± 0.39	0.35 ± 0.16
ACS/CLEAR	2005	1.64 ± 0.18	0.35 ± 0.05
ACS/CLEAR	2006	1.29 ± 0.19	0.32 ± 0.08
ACS/F475W	2003–2006	1.93 ± 0.63	0.40 ± 0.15
ACS/F475W	2003	2.32 ± 1.15	0.37 ± 0.45
ACS/F475W	2004	2.12 ± 1.78	0.80 ± 0.83
ACS/F475W	2005	1.67 ± 1.92	0.44 ± 0.24
ACS/F475W	2006	1.63 ± 0.88	0.21 ± 0.12
ACS/F606W	2003–2006	1.70 ± 0.42	0.41 ± 0.12
ACS/F606W	2003	2.36 ± 0.82	0.16 ± 0.23
ACS/F606W	2004	0.65 ± 1.69	1.38 ± 0.64
ACS/F606W	2005	1.21 ± 0.57	0.70 ± 0.13
ACS/F606W	2006	1.39 ± 0.57	0.31 ± 0.15
ACS/F775W	2005–2006	1.44 ± 0.65	0.45 ± 0.22
ACS/F775W	2005	2.10 ± 1.05	0.23 ± 0.26
ACS/F775W	2006	1.14 ± 0.77	0.62 ± 0.27
ACS/F814W	2003–2006	1.66 ± 0.57	0.11 ± 0.17
ACS/F814W	2003	1.97 ± 1.09	0.24 ± 0.49
ACS/F814W	2004	1.40 ± 0.97	X
ACS/F814W	2005	1.57 ± 0.50	X
ACS/F814W	2006	1.47 ± 0.58	0.16 ± 0.29
ACS/F850LP	2006	0.89 ± 0.75	X
WFPC2/F450W	2007	6.7 ± 1.2	0.97 ± 0.80
WFPC2/F606W	2007	3.49 ± 0.21	1.2 ± 0.6
WFPC2/F814W	2007	3.76 ± 0.24	1.41 ± 0.25
WFPC2/F850LP	2007	4.0 ± 0.8	1.0 ± 0.7
WFC3/F350LP	2011–2013	1.87 ± 0.38	X
WFC3/F350LP	2011	1.94 ± 0.25	X
WFC3/F350LP	2012	1.51 ± 0.60	X
WFC3/F350LP	2013	1.95 ± 0.88	X
WFC3/F475W	2010	1.70 ± 0.76	X
WFC3/F606W	2010	2.16 ± 0.48	X
WFC3/F814W	2010	1.46 ± 0.38	X
WFC3/F845W	2009–2010	1.22 ± 0.68	X
WFC3/F845W	2009	1.21 ± 0.68	X
WFC3/F845W	2010	1.82 ± 0.64	X

longitude, do show rings at the right locations (Figure 15). We therefore omitted the 4.8 μm data points from the spectra, and replaced the 4.6 μm data point for the ν ring with an upper limit sign. Moreover, we did not plot the HST/WFPC2 measurements due to their large uncertainties (Section 3.4).

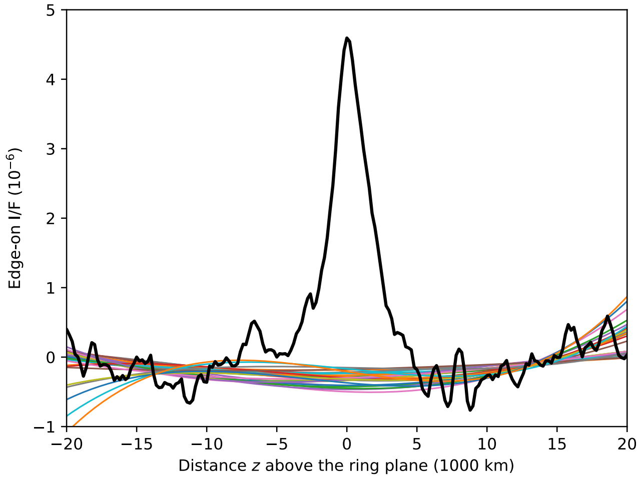

Figure 20. HST/WFPC2: A vertical profile across the core of the μ ring from the Wide Field/Planetary Camera 2 data set. As with the radial profiles of the ν ring (Figure 18), a variety of polynomial models are fitted to the samples outside the ring's limits, although in this case we have an edge-on, vertical profile rather than a radial profile. The area under the curve, after subtracting off the background model, is the VIF.

The reflectance spectra in Figure 22 clearly confirm the blue color of the μ ring, as well as the red color of the ν ring (de Pater, Hammel, et al., 2006). Most intriguing are the dip in both rings at $\sim$3 μm and, for only the μ ring, a peak at $\sim$3.5 μm. The low 3-μm intensity is also obvious from the scans in Figure 15. We did not include the extremely broad F150W2 and F322W2 filters on the graph; interpretation of these broad filters is difficult because it averages over potential spectral features. We note, though, that the F322W2 filter values fall right between the F277W and F356W filter points for both rings (Table 5).

Reflectance spectra of water-ice features on solid surfaces typically show an absorption band at $\sim$3 μm, with a small Fresnel peak at 3.1 μm and a peak at 3.6 μm (Bockelée-Morvan et al., 2024; Emery et al., 2024; Hedman et al., 2024; Protopapa et al., 2024). The blue slope of the μ ring spectrum suggests the ring to be composed of (sub-)micron-sized grains, while the 3-μm absorption plus 3.6-μm peak suggest that these tiny grains are composed of water-ice. To strengthen our conclusion we superpose a spectrum for (sub-)micron-sized icy grains on the graph. This spectrum was created with Python's PyMieScatt module (Appendix B; Sumlin et al. (2018); Sumlin (2025)), assuming a differential particle size distribution D^{-q} with $q = 3$ and minimum and maximum diameters $D_{\min} = 0.02$ μm and $D_{\max} = 1000$ μm (although the model is not strongly sensitive to these limits). All particles are composed of water-ice, using optical constants from (Warren & Brandt, 2008). Although the spectrum is not a "best-fit" to the observations, it clearly suggests a preponderance of tiny grains, yet also the presence of larger (100's of μm) sized particles. As shown, changing to $q = 3.5$ makes the spectrum too steep, and $q = 2.5$ makes it too flat. Also, using a much smaller value of $D_{\max}$ ($\lesssim$50 μm) decreases the 3.6 μm emission peak. Of course, the size distribution does not necessarily need to follow an exact power-law, and the 3.6 μm emission bump might indicate a flatter power law at the larger sizes.

The 3-μm absorption feature for the ν ring appears to be slightly shifted toward longer wavelengths, and does not show the 3.6-μm emission peak. The red spectral slope is suggestive of a size distribution with a slope that is less steep than that of the μ ring. The absorption feature does not seem to be produced by water-ice, but rather by organics. The model spectrum superposed on the ν ring data in Figure 22 is for a particle size distribution with $q = 2$, $D_{\min} = 0.2$ μm, and $D_{\max} = 1000$ μm. We adopted a rocky-like refractive index with $n = 1.6$ and an imaginary part $k = 3 \times 10^{-3}$. We also experimented with a fractional contribution of tholins (Khare et al., 1984) ranging from 5% to 20%. Although we did not explore the full parameter space (q, $D_{\min}$, $D_{\max}$, $n + ik$ and its wavelength dependence, and tholin fraction), our results are consistent with this being a regular dusty ring composed of rocky material and 10%–15% tholins. As with the μ ring, changing q alters the slope of the spectrum, making it too flat for $q = 1.5$, and too flat longwards of 1 μm for $q = 2.5$. A several (e.g., 5) times smaller $D_{\max}$ results in too steep a slope.

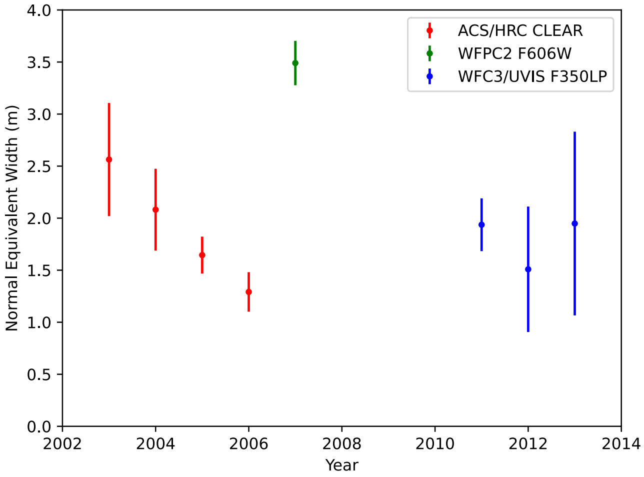

Figure 21. HST/ACS: Measurements of the μ ring versus year as obtained by HST through its broadest filters. Plotted error bars are one sigma.

4.2. Optical Depths of the Rings

In the discussion of Figure 22 above, we have compared the overall shape of the plotted spectra to models generated for small Mie-scattering particles. As discussed in Appendix B, the inferred scale factor on our Mie scattering models enables us to derive a direct estimate of the peak normal optical depth τ_0 for each ring. For the μ ring, our best match to the spectral shape implies that $q = 3$. With $\mu I/F = 3.5 \times 10^{-7}$ in JWST filter F150W (1.5 μm), we find the normal optical depth $\tau_0 \approx 1.1 \times 10^{-5}$. For the ν ring, with $\mu I/F = 6 \times 10^{-7}$ in F150W and a particle size distribution with $q = 2$, we obtain $\tau_0 \approx 3 \times 10^{-5}$. Precise uncertainties are difficult to assess, however, because they are deeply interwoven with other uncertainties (in q, limits of the size distribution, refractive index, composition, and other aspects of the ring modeling).

It is instructive to compare these values to a simpler model for the relationship between I/F and τ_0, discussed in Equations 6–8 of de Pater et al. (2013):

$$\mu\, I/F = A\tau_0, \tag{7}$$

and:

$$A = \frac{1}{4}\,\varpi P(\theta = 180°), \tag{8}$$

Here, A is the geometric albedo, ϖ is the single scattering albedo, and P is the phase function at scattering angle $\theta = 180° - \alpha$ (with α the solar phase angle). These equations are most often used in the limit of particles much larger than the wavelength of light, although they can often be extended to smaller particles. The phase function P is often parameterized as:

$$P(\theta) = \frac{1 - g^2}{\left[1 + g^2 - 2g\cos(\theta)\right]^{3/2}}, \tag{9}$$

which is normalized so that its integral over 4π steradians equals 4π. At $\theta = 180°$, this reduces to:

$$P(\theta) = \frac{1 - g}{(1 + g)^2}. \tag{10}$$

Here, g is the Henyey-Greenstein asymmetry parameter, which is equal to zero for isotropic scattering and one for perfect forward-scatter. A typical value for dust is ~0.7, while for sub-micron sized material g can be much smaller (see Appendix in de Pater et al. (2013)).

Our Mie-scattering results for the μ ring imply $A = 0.032$ via Equation 7. Because the imaginary component of the refractive index of water ice is small at 1.5 μm, we expect $\varpi \approx 1$. This, in turn, implies $P = 0.13$ and $g \approx 0.65$, a plausible value for a forward-scattering ring composed almost exclusively of fine dust. Similarly, for the ν ring, $A = 0.023$, so $P = 0.09$ if $\varpi \approx 1$, and $g \approx 0.72$. These values for g are indeed indicative of dust, and the slightly

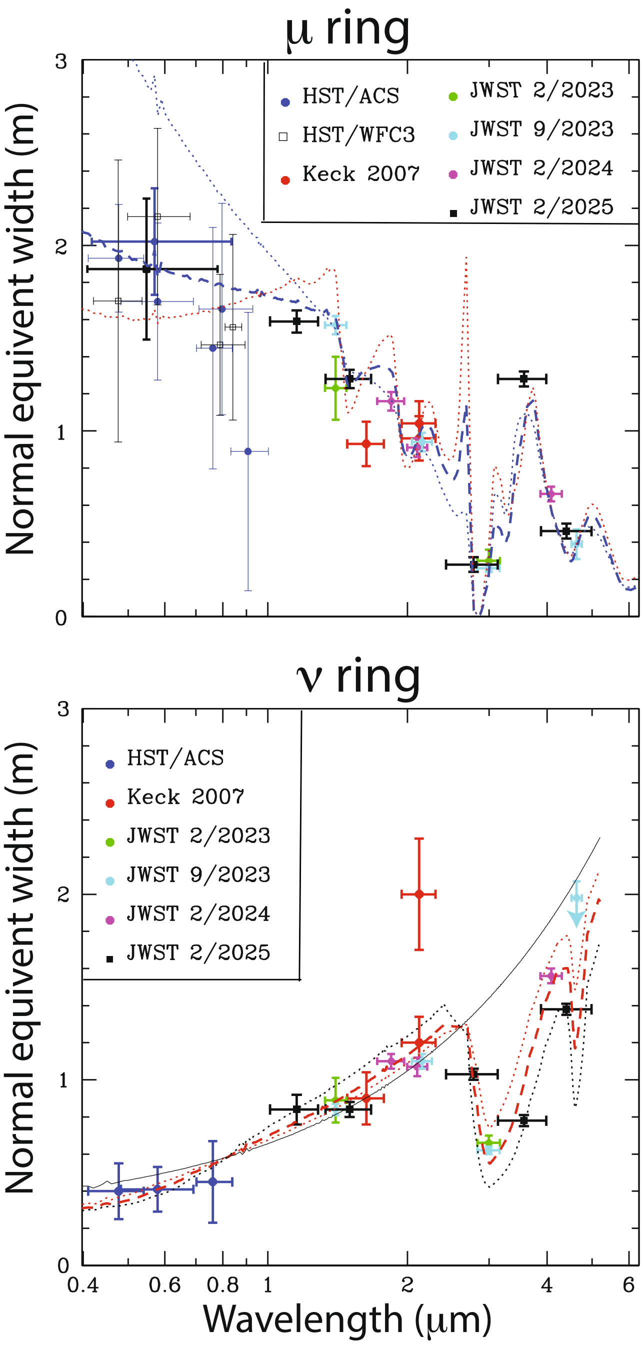

Figure 22.

Figure 22. Spectra of the Uranian outer rings, constructed from the Keck, James Webb Space Telescope (JWST) and Hubble Space Telescope (HST) data in Table 4 (Columns 8 and 10), Table 5 (Columns 4 and 6), and Table 6. The JWST uncertainties in the plot are those of the data (Columns 3 and 5), which are more realistic than the model fit uncertainties. We did not plot the broad-band JWST filters which overlap the narrower filters, nor the HST/Wide Field/Planetary Camera 2 and the JWST F480M data, while the F460M ν ring data point is shown as an upper limit (see Section 3.3 for details). Models are superposed. The μ ring: particle size distribution for a water-ice spectrum with $D = 0.02 - 1000\,\mu$m, and $q = 3$ (blue dashed line), $q = 2.5$ (dotted red line), and $q = 3.5$ (dotted blue line). The ν ring model is composed of rocky grains ($n = 1.6$, $k = 3 \times 10^{-3}$), $D = 0.2 - 1000\,\mu$m, and $q = 2$ (solid thin black line). Additional models containing tholin fractions of 5%, 10%, and 20% (dotted red, dashed red, and dotted black lines) are shown, which capture the observed dip around 3 μm. All spectra are calculated for a solar phase angle of 3°, similar to the JWST observations.

smaller value for the μ ring compared to the ν ring, assuming the same single scattering albedo, is consistent with the μ ring being composed of smaller-sized particles (having a size distribution with $q = 3$) than the ν ring (with $q = 2$). In other words, the ν ring is somewhat more forward-scattering than the μ ring, which is compatible with the idea that the μ ring has a larger component of sub-micron grains, which have a more symmetric phase function.

4.3. Shape and Orbits of the Rings

As shown in Figures 13 and 14, both rings cover the full longitude range, and do not show evidence for longitudinal brightness variations, as were originally suggested for the ν ring based upon HST observations (Showalter & Lissauer, 2006).

As shown in Figure 8, the ν ring is relatively narrow and centered at a Uranian distance of ~67,450 km, in between the moons Portia and Rosalind at 66,100 km and 69,900 km, respectively. Its total extent is ~3000 km, with a full width at half maximum intensity, FWHM, of ~500 km, and a lower intensity outward extension. This outward extension might be caused by a radial distribution of the source material of this ring.

In the near infrared, the μ ring extends over a radial range from ~90,000 to ~101,000 km, with its center at ~97,560 km (Figure 8). It has a FWHM of ~2350 km, and is characterized by a low-intensity triangular-shaped inward extension, together with a slight outward extension. The extent is slightly broader at visible wavelengths (see discussion in Section 4.4). The roughly triangular shapes of both rings agree well with those observed with HST and Voyager (Showalter & Lissauer, 2006).

The μ ring's outward extension might be the result of plasma drag, since the radius of the synchronous orbit, $R_{\mathrm{syn}} = 82{,}700$ km (assuming Uranus' rotation period is 17.24 hr), lies interior to the μ ring. Any other drag forces (e.g., radiation pressure) would slow down the motion of orbiting particles, and hence result in inward extensions of the rings; such forces may explain the μ ring's inward extension.

Judging from Figure 14 (in particular the F115W, F150W and F150W2 filters) the μ ring may be eccentric, because it does not follow a straight line. It is difficult, though, to determine eccentricities with high precision, both because of the relatively low spatial resolution (~2 pixels, or close to 1,000 km at the short wavelengths) and because a tiny error in the center position of Uranus, despite our best efforts to navigate the image, would distort the rings in a similar way. However, the μ ring appears to be slightly more distorted than the ν ring (Figure A3). If we assume the distortions in both rings can be completely attributed to orbital eccentricities, we find eccentricities of order 0.0035 for the μ ring and 0.0025 for the ν ring. Hence, it is clear that any eccentricity in these rings must be equal to or less than these values. If the orbit of the ν ring would be circular, the μ ring may show an eccentricity of order 0.001. Nevertheless, we regard these values as upper limits on the eccentricity, pending the availability of better data.

As shown in column 4 of Table 4, the μ ring's VIF$_\mu$ remains essentially the same at 2 μm between $B = 0.62°$ and 0.27°, as expected for rings with an optical depth $\tau_0 \lesssim$ a few times 10^{-4}, the upper limit determined for the μ ring (Section 4.2). For rings with a larger optical depth, like the ζ ring with $\tau_0 = 0.0045$, one can determine the ring's physical thickness from the decrease in VIF with B (see Figure 15 of de Pater et al. (2013)). Unfortunately, the μ ring is too optically thin for us to be able to constrain its physical vertical extent.

In contrast, observations of the ν ring show an increase in VIF$_\nu$ and hence NEW$_\nu$ (see the high point in Figure 22) by about 50% between B = 0.62° and 0.27°. Although one could explain an increase in a ring's peak brightness, the VIF should either remain the same or decrease when approaching zero. After having convinced ourselves that all moonlets moving through the data had been properly removed, this increase in intensity may suggest longitudinal and/or time variations in this ring. For example, an impulse of dust (due, e.g., to an impact) would temporarily brighten only a section of the ring. However, in the absence of any other observations that suggest such a process is at work in the ν ring, we must regard this measurement as unexplained.

4.4. Origin of the Rings

The ν ring appears to be a relatively conventional dusty, red ring, like the rings of Jupiter and Saturn′s G ring. As shown in Section 4.1, the ν ring spectrum can be matched by a differential size distribution D^{-q} with $q = 2$, and an index of refraction similar to that of rocks ($n = 1.6$, $k = 3 \times 10^{-3}$). The broad spectral feature at 3 μm is strongly suggestive of a 10%–15% composition of organics, like tholins. The exponent of $q = 2$ is close to the value of $q = 2.5$ expected for a collisionally evolved population of bodies. Although we expect one or more parent bodies embedded in the ν ring to explain its existence (unless the ring is ephemeral), such bodies have not (yet) been found.

As discussed in Section 4.1, the μ ring most likely consists of (sub-)micron sized grains composed of water-ice. This ring probably originates from the moon Mab, which orbits Uranus near the center of the μ ring (Showalter & Lissauer, 2006). This moon was suggested to be a small (6-km radius) icy moon (de Pater, Hammel, et al., 2006; Molter et al., 2023; Paradis et al., 2023), as recently been confirmed from an analysis of JWST data (Hedman et al., 2025). The ring might be produced via micrometeoroid impacts on Mab (de Pater, Hammel, et al., 2006). Since (sub)-micron sized grains are more susceptible to the effects of the planet's oblateness (J_2), radiation pressure and electromagnetic forces (Burns et al., 1979, 2001; Hamilton & Burns, 1994; Horanyi et al., 1992), tiny grains ejected from Mab will spread out radially and vertically, while the larger grains will stay in Mab's orbit and may be re-accreted by Mab; hence the surviving predominantly sub-micron sized grains produce the blue color and radial extent of the μ ring as observed. The evolution of small versus larger grains for the μ ring has been confirmed via numerical simulations by Sfair and Giuliatti Winter (2012). The slightly larger radial extent seen in the HST visible wavelength data than with JWST in the near-infrared, can naturally be explained by this theory as well; at visible wavelengths we are sensitive to somewhat smaller grains than in the infrared. These smaller grains, being more susceptible to the non-gravitational forces, are spread out over a broader radial extent.

As shown by the HST data, the μ ring decreased in brightness (NEW_{μ}) by roughly 50% between 2003 and 2006. The time frame suggests that the lifetime of the μ ring's smallest dust grains is on the order of years or shorter. It also requires that the source function for the ring varies on this time scale. The specific reasons for such variations are unclear. Perhaps a recent, larger meteoroid impact into Mab, or a mutual collision between two larger ring members, yielded a sudden injection of dust into the ring; the ring would show a sudden increase in brightness after such an event, which would be followed by a steady decay back to its long-term, steady-state value.

We note that the μ ring continues to show notable parallels to Saturn's E ring, which is also centered on a moon (Enceladus), has a similarly peaked radial profile, a blue color, and time-variations. The parallel seemingly breaks down, however, because Enceladus is known to emit plumes of fine dust into the E ring, whereas Mab, at ∼6 km radius (de Pater, Hammel, et al., 2006; Hedman et al., 2025; Molter et al., 2023; Paradis et al., 2023; Showalter & Lissauer, 2006), is seemingly far too small to be active. However, we note that Centaurs orbit at similar distances from the Sun and show time-variable activity (Poppe, 2019), perhaps serving as a Mab analog. It is perhaps also notable that the dust in the coma of at least one Centaur, 174P/Echeclus, appears to be blue (Seccull et al., 2019).

5. Conclusions

We observed Uranus's μ and ν rings in July-August 2007 with NIRC2 on the Keck telescope at 2.12 and 1.63 μm when the ring plane was almost edge-on as seen from Earth. We extended this data set with HST data at visible wavelengths at different ring opening angles ($B \sim -17°$ to $25°$), and with JWST/NIRCam images taken at 1.4–4.8 μm and $B \sim 60°$.

We examined scans through the rings, averaged over a radial distance 73,500–98,500 km for the μ ring and 60,740–67,740 km for the ν ring in the edge-on Keck data, and averaged over longitude for the JWST/NIRCam observations. For the Keck data these scans yield the vertically integrated I/F (VIF). The JWST data were used to determine the equivalent width, EW. The latter data were converted to the normal EW, NEW, by multiplying the observed value by $\mu = \sin(B)$. The VIF was converted to NEW by modeling the geometry of a face-on and edge-on ring, and assuming that the brightness varies in proportion to the path length through the rings. Our main conclusions are summarized as follows:

- We confirmed (de Pater, Hammel, et al., 2006)) that the μ ring is blue, and the ν ring red.
- Based upon both the blue slope of its spectrum and the presence of an absorption feature near 3 μm and emission near 3.6 μm, we suggest the μ ring to be composed of (sub-)micron sized icy grains, originating most

likely via micrometeoroid impacts on the moon Mab. This, in turn, is an indirect confirmation that Mab is a relatively ice-rich moon.

- The red slope of the ν ring suggests that this ring is a dusty ring. The 3-μm absorption feature in this ring is indicative of organic materials, like tholins. A reasonable match to the observed spectrum is obtained for rocky bodies ($n = 1.6$, $k = 3 \times 10^{-3}$), with a 10%–15% contribution of tholins, and a size distribution D^{-q} with $q = 2$.
- The radial profiles of both rings are roughly triangular in shape. The rings are characterized by a narrow core, with lower intensity extensions, on the inside and outside for the μ ring, and outside only for the ν ring. These shapes are very similar to those observed at the time with HST and Voyager (Showalter & Lissauer, 2006). The inward extension of the μ ring appears to be slightly broader in the HST (visible wavelengths) data than in the JWST near-infrared observations, which is consistent with the theory that the μ ring may originate from micrometeoroid impacts on the moon Mab.
- The normal equivalent width, NEW, is of order 1 m at infrared wavelengths for both rings, up to 2 m in the visible for the μ ring. We determined the normal optical depth of the rings at 1.5μm to fit the spectra. We find $\tau_0 \approx 10^{-5}$ for the μ ring and $\tau_0 \approx 3 \times 10^{-5}$ for the ν ring. The μ ring appears to be somewhat less forward-scattering than the ν ring, which is consistent with the idea that it is composed of generally smaller particles.
- The μ ring intensity, or NEW, at visible wavelengths (HST/ACS data) appeared to decrease by roughly 50% between 2003 and 2006; although the precise mechanism driving its time variations remains unclear, a meteoroid impact or collisions between larger-sized chunks of ice could cause a brightening prior to 2003 like this.

A more comprehensive understanding of Uranus's outer ring system, particularly its faint, dusty components like the μ and ν rings, will likely depend on direct, in situ observations. Such data may only become available through the Uranus Orbiter and Probe (UOP) mission, which was identified as the highest-priority flagship mission in the National Academies' 2023 Planetary Science and Astrobiology Decadal Survey (National Academies of Sciences & Medicine, 2022). Equipped with advanced imaging and dust-detection instruments, UOP would enable detailed mapping of ring structure, composition, and dynamics, offering more detailed results that are inaccessible from Earth and space-based telescopes.

Appendix A: Figures A1–A3

Three figures are shown in this Appendix: Figure A1: A comparison of PSF images in the F210M filter as observed in our data in the form of Miranda (panel a), and as downloaded from https://stsci.app.box.com/v/jwst-simulated-psf-library/folder/174723156124 (panel b). Figure A2 shows 1-D scans through the PSFs in different filters. Figure A3 shows the radius of the μ and ν rings as derived from Figure 14 (Figure A3).

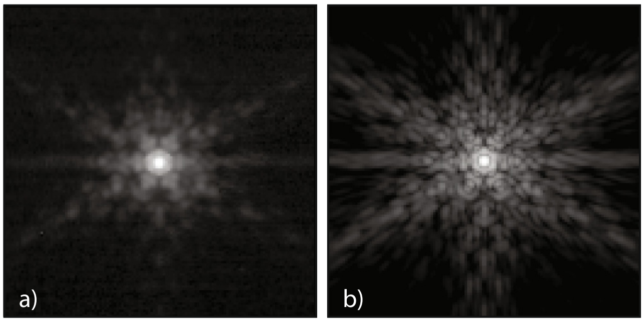

Figure A1. JWST: Two point spread function (PSF) images in the F210M filter. (a) Miranda as observed simultaneously with the Uranian system. (b) A PSF as downloaded from STSci (https://stsci.app.box.com/v/jwst-simulated-psf-library/folder/174723156124).

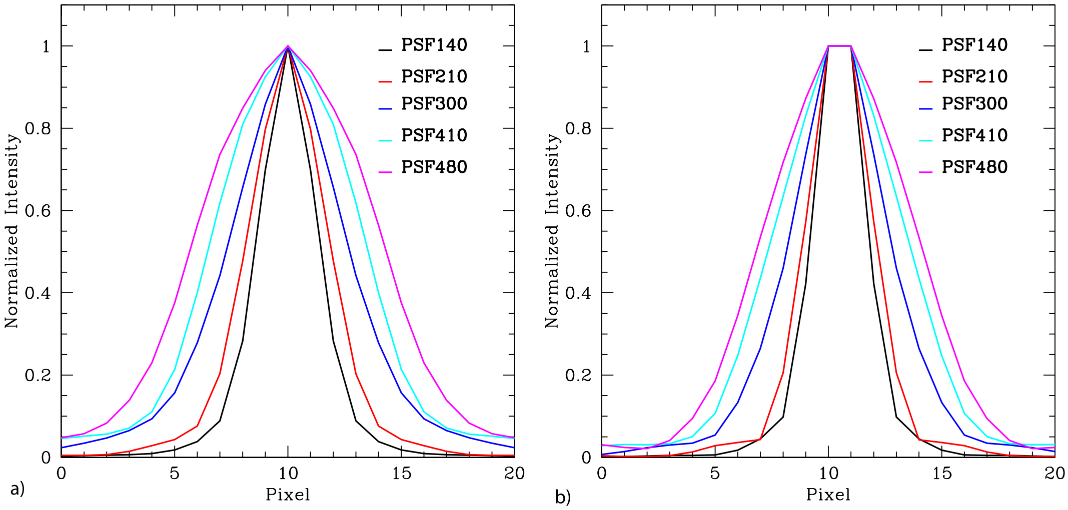

Figure A2. JWST: 1-D point spread function scans in several filters as indicated. (a) PSFs constructed from images of Miranda. (b) PSFs constructed from the JWST-provided PSFs (https://stsci.app.box.com/v/jwst-simulated-psf-library/folder/174723156124). The PSFs as shown here were adjusted to the same scale as our ring scans (334.448 km/pixel) using the congrid function in IDL, and averaged over azimuth.

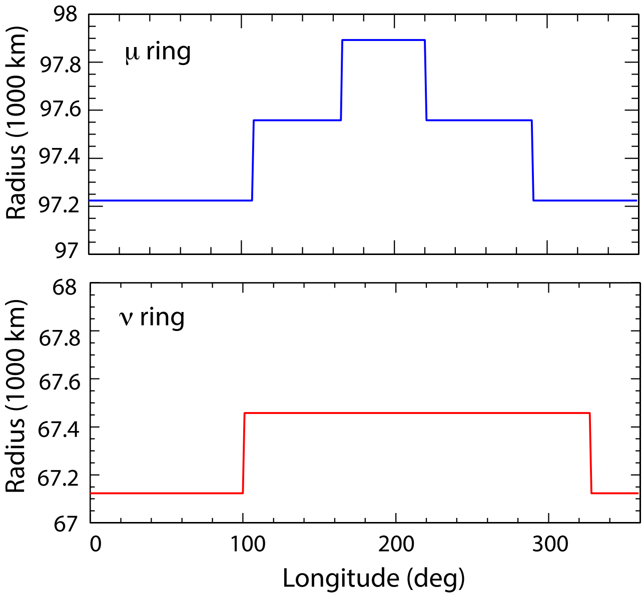

Figure A3. JWST: The radius of the μ and ν rings as derived from Figure 14. The incremental steps in the y-direction are 1 pixel.

Appendix B: Mie Scattering

In Section 4.1 we matched a model spectrum to the data, using the Python module PyMieScatt (Sumlin, 2025; Sumlin et al., 2018) to generate the models. In the following we show how we used and interpreted the results from this code.

We observed the ring's reflectivity (Showalter, 1985):

$$\frac{I}{F} = \int \frac{\pi r^2}{4} Q_{scatt}(r)\, P(\theta, r) n(r) dr \tag{B1}$$

where πF is the solar flux at Uranus's distance, n the number density of particles with radius r per unit area (i.e., column density), Q_{scatt} the scattering efficiency, and $P(\theta, r)$ is the scattering phase function with θ the scattering angle. The phase function is normalized to 4π when integrated over 4π steradians:

$$P(\theta) = \frac{\int \pi r^2 Q_{scatt}(r)\, P(\theta, r)\, n(r) dr}{\int \pi r^2 Q_{scatt}(r)\, n(r) dr}. \tag{B2}$$

The optical depth can be written as:

$$\tau_0 = \int \pi r^2 Q_{ext}(r) n(r) dr, \tag{B3}$$

with Q_{ext} the extinction efficiency.

The PyMieScatt module follows somewhat different conventions, using somewhat different terminology; one must therefore exercise caution when relating its outputs to the quantities defined above. The function SF_SD returns the phase function for a distribution of particle sizes, but with different normalization than Equation B2. We determined, empirically, that it returns a quantity we call:

$$P_{SF\_SD} = P(\theta) \beta'_{scatt} \frac{\pi}{\lambda^2}, \tag{B4}$$

where:

$$\beta'_{scatt} = \int \pi r^2 Q_{scatt}(r)\, n(r) dr. \tag{B5}$$

Combining the above equations, we find that:

$$\frac{I}{F} = P_{SF\_SD} \times \frac{\lambda^2}{4\pi}, \tag{B6}$$

Meanwhile, the function Mie_SD returns quantities called β_{scatt} and β_{ext} which, according to the documentation (and confirmed by extensive testing), match our definitions of β'_{scatt} and τ_0 except for a fixed scale factor of 10^6 ($\beta'_{ext} = 10^6 \times \beta_{ext}$). This enables us to define the relationship between I/F and τ_0 from the function outputs:

$$\tau_0 = \frac{I}{F} \times \left[\frac{4\pi}{\lambda^2} \frac{10^6\, \beta_{ext}}{P_{SF\_SD}} \right], \tag{B7}$$

where I/F is the observed reflectivity at wavelength λ. The module represents particle sizes by diameter D rather than radius, and it uses units of nm. The models in Section 4.1 are all based on power laws of the form $n \propto D^{-q}$ over a specified range of diameters $D_{\min}$ to $D_{\max}$.

Conflict of Interest

The authors declare no conflicts of interest relevant to this study.

Availability Statement

The JWST data were downloaded from the Mikulski Archive for Space Telescopes at the Space Telescope Science Institute, as part of the Cycle 1 Outreach Campaign, Director's Discretionary program #2739 (PI: Klaus M. Pontoppidan), Cycle 2's GTO program #2768 (PI: Naomi Rowe-Gurney), and Cycle 3's GO program #6379 (PI: Maryame El Moutamid). We used the *i2d*.fits files, which were deprojected using the deprojection software (Jupyter notebook) on Zenodo (Hedman & de Pater, 2025). Once deprojected, they were further processed in IDL, as described in the text. Jupyter notebooks to fit the μ and ν ring spectra are also uploaded to Zenodo (Hedman &

de Pater, 2025). The Keck data were obtained from the Keck Archive (https://koa.ipac.caltech.edu for the dates 20070726, 20070727, 20070808, and 20070809). The HST data were downloaded from the Mikulski Archive for Space Telescopes at the Space Telescope Science Institute (ACS/HRC: #9823, 10102, 10473, 10534, 10805, 10870; WFPC2/PC1: #10870, 11118, 11292. WFC3/UVIS: #11630, 12245, 12665, 13055). Python notebooks and support files describing the HST data analysis can be found on Zenodo (Showalter, 2026). The final Keck images are uploaded to Zenodo (de Pater, 2025).

Acknowledgments

We thank Richard Jerousek and Shawn M. Brooks for constructive comments on the manuscript. Some of the data presented in this paper were obtained at the W.M. Keck Observatory, which is operated as a scientific partnership among the California Institute of Technology, the University of California, and the National Aeronautics and Space Administration. The Observatory was made possible by the generous financial support of the W.M. Keck Foundation. The authors wish to recognize and acknowledge the very significant cultural role and reverence that the summit of Maunakea has always had within the indigenous Hawaiian community. Without their generous hospitality, we would not have been able to obtain the observations presented here. This research was funded by NASA's Solar System Observations (SSO) award NNX16AK14G to the University of California. Fletcher was supported by STFC Grant reference UKRI1205. For the purpose of open access, the author has applied a Creative Commons Attribution (CC BY) license to the Author Accepted Manuscript version arising from this submission. We also used observations made with the NASA/ESA/CSA James Webb Space Telescope. These data were obtained from the Mikulski Archive for Space Telescopes at the Space Telescope Science Institute, which is operated by the Association of Universities for Research in Astronomy, Inc., under NASA contract NAS 5–03127 for JWST and NAS5-26555 for HST. The JWST observations are associated with programs #2739, #2768 and #6379. Support for HST Program numbers 9823, 10102, 10473, 10870, 11292, 12245, 12665, 13055. was provided by NASA through a Grant from the Space Telescope Science Institute, which is operated by the Association of Universities for Research in Astronomy, Incorporated, under NASA contract NAS5-26555.

References

Acton, C., Bachman, N., Semenov, B., & Wright, E. (2018). A look towards the future in the handling of space science mission geometry. *Planetary and Space Science*, *150*, 9–12. https://doi.org/10.1016/j.pss.2017.02.013

Acton, C. H. (1996). Ancillary data services of NASA's navigation and ancillary information facility. *Planetary and Space Science*, *44*(1), 65–70. https://doi.org/10.1016/0032-0633(95)00107-7

Bockelée-Morvan, D., Lellouch, E., Poch, O., Quirico, E., Cazaux, S., de Pater, I., et al. (2024). Composition and thermal properties of Ganymede's surface from JWST/NIRSpec and MIRI observations. *Astronomy and Astrophysics*, *681*, A27. https://doi.org/10.1051/0004-6361/202347326

Burns, J. A., Hamilton, D. P., & Showalter, M. R. (2001). Dusty rings and circumplanetary dust: Observations and simple physics. In *Interplanetary dust*.641

Burns, J. A., Lamy, P. L., & Soter, S. (1979). Radiation forces on small particles in the solar system. *Icarus*, *40*(1), 1–48. https://doi.org/10.1016/0019-1035(79)90050-2

Bushouse, H., Greenfield, P., & Miller, T. (2012). The JWST calibration reference data system. In P. Ballester, D. Egret, & N. P. F. Lorente (Eds.), *Astronomical data analysis software and systems xxi* (Vol. 461).737

Colina, L., Bohlin, R. C., & Castelli, F. (1996). The 0.12-2.5 micron absolute flux distribution of the sun for comparison with solar analog stars. *The Astronomical Journal*, *112*, 307. https://doi.org/10.1086/118016

de Pater, I. (2025). Final keck Uranus 2007 RPX images of the mu and nu rings [Dataset]. https://doi.org/10.5281/ZENODO.17755760

de Pater, I., Davies, A. G., McGregor, A., Trujillo, C., Ádámkovics, M., Veeder, G. J., et al. (2014). Global near-IR maps from Gemini-N and keck in 2010, with a special focus on janus Patera and kanehekili Fluctus. *Icarus*, *242*, 379–395. https://doi.org/10.1016/j.icarus.2014.06.019

de Pater, I., Dunn, D. E., Stam, D. M., Showalter, M. R., Hammel, H. B., Min, M., et al. (2013). Keck and VLT AO observations and models of the uranian rings during the 2007 ring plane crossings. *Icarus*, *226*(2), 1399–1424. https://doi.org/10.1016/j.icarus.2013.08.001

de Pater, I., Gibbard, S. G., & Hammel, H. B. (2006). Evolution of the dusty rings of Uranus., *180*(1), 186–200. https://doi.org/10.1016/j.icarus.2005.08.011

de Pater, I., Hammel, H. B., Gibbard, S. G., & Showalter, M. R. (2006). New dust belts of Uranus: One ring, two ring, red ring, blue ring. *Science*, *312*(5770), 92–94. https://doi.org/10.1126/science.1125110

de Pater, I., Hammel, H. B., Showalter, M. R., & Van Dam, M. A. (2007). The dark side of the rings of Uranus. *Science*, *317*(5846), 1888–1890. https://doi.org/10.1126/science.1148103

Emery, J. P., Wong, I., Brunetto, R., Cook, J. C., Pinilla-Alonso, N., Stansberry, J. A., et al. (2024). A tale of 3 dwarf planets: Ices and organics on sedna. *Gonggong, and Quaoar from JWST spectroscopy*, *414*, 116017. https://doi.org/10.1016/j.icarus.2024.116017

Gardner, J. P., Mather, J. C., Abbott, R., Abell, J. S., Abernathy, M., Abney, F. E., et al. (2023). The James Webb Space telescope mission. *Publications of the Astronomical Society of the Pacific*, *135*(1048), 068001. https://doi.org/10.1088/1538-3873/acd1b5

Gibbard, S. G., de Pater, I., & Hammel, H. B. (2005). Near-infrared adaptive optics imaging of the satellites and individual rings of Uranus. *Icarus*, *174*(1), 253–262. https://doi.org/10.1016/j.icarus.2004.09.008

Greenfield, P., & Miller, T. (2016). The calibration reference data system. *Astronomy and Computing*, *16*, 41–53. https://doi.org/10.1016/j.ascom.2016.04.001

Greisen, E. W., & Calabretta, M. R. (2002). Representations of world coordinates in FITS. *Astronomy and Astrophysics*, *395*(3), 1061–1075. https://doi.org/10.1051/0004-6361:20021326

Hamilton, D. P., & Burns, J. A. (1994). Origin of saturn's E ring: Self-sustained, naturally. *Science*, *264*(5158), 550–553. https://doi.org/10.1126/science.264.5158.550

Hammel, H. B., Baines, K. H., & Bergstrahl, J. T. (1989). Vertical aerosol structure of Neptune: Constraints from Center- to- Limb Profiles. *Icarus*, *80*(1), 416–438. https://doi.org/10.1016/0019-1035(89)90149-8

Hedman, M. M., & de Pater, I. (2025). Jupyter notebooks for JWST uranian ring data [Software]. https://doi.org/10.5281/zenodo.17765232

Hedman, M. M., de Pater, I., Cartwright, R., El Moutamid, M., DeColibus, R., Showalter, M., & Hammel, H. B. (2025). Spectral trends across the rings and inner moons of Uranus and Neptune from JWST NIRCam images. *arXiv e-prints, arXiv:2506.18650*. https://doi.org/10.48550/arXiv.2506.18650

Hedman, M. M., Tiscareno, M. S., Showalter, M. R., Fletcher, L. N., King, O. R. T., Harkett, J., et al. (2024). Water-ice dominated spectra of Saturn's rings and small moons from JWST. *Journal of Geophysical Research (Planets)*, *129*(3), e2023JE008236. https://doi.org/10.1029/2023JE008236

Horanyi, M., Burns, J. A., & Hamilton, D. P. (1992). The dynamics of Saturn's E ring particles. *Icarus*, *97*(2), 248–259. https://doi.org/10.1016/0019-1035(92)90131-P

Huff, L. W. (2005). NIRCam instrument optics. In J. B. Heaney & L. G. Burriesci (Eds.), *Cryogenic optical systems and instruments xi* (Vol. 5904, pp. 30–37). https://doi.org/10.1117/12.619909

Khare, B. N., Sagan, C., Arakawa, E. T., Suits, F., Callcott, T. A., & Williams, M. W. (1984). Optical constants of organic tholins produced in a simulated Titanian atmosphere: From soft x-ray to microwave frequencies. *Icarus*, *60*(1), 127–137. https://doi.org/10.1016/0019-1035(84)90142-8

Lupton, R. H., Gunn, J. E., & Szalay, A. S. (1999). A modified magnitude system that produces well-behaved magnitudes, colors, and errors Even for low signal-to-noise ratio measurements. *The Astronomical Journal*, *118*(3), 1406–1410. https://doi.org/10.1086/301004

Molter, E. M., de Pater, I., & Moeckel, C. (2023). Keck near-infrared detections of mab and perdita. *Icarus*, *405*, 115697. https://doi.org/10.1016/j.icarus.2023.115697

National Academies of Sciences, E, & Medicine (2022). Origins, worlds, and life: A decadal strategy for planetary science and astrobiology 2023–2032. *The National Academies Press*. https://doi.org/10.17226/26522

Paradis, S., Moeckel, C., & de Pater, I. (2023). Near-IR photometry of the small Uranian satellites with keck at phase angles 0–2°. *Icarus*, *391*, 115331. https://doi.org/10.1016/j.icarus.2022.115331

Poppe, A. R. (2019). The contribution of Centaur-emitted dust to the interplanetary dust distribution. *Monthly Notices of the Royal Astronomical Society*, *490*(2), 2421–2429. https://doi.org/10.1093/mnras/stz2800

Protopapa, S., Raut, U., Wong, I., Stansberry, J., Villanueva, G. L., Cook, J., et al. (2024). Detection of carbon dioxide and hydrogen peroxide on the stratified surface of charon with JWST. *Nature Communications*, *15*(1), 8247. https://doi.org/10.1038/s41467-024-51826-4

Rieke, G. H., Blaylock, M., Decin, L., Engelbracht, C., Ogle, P., Avrett, E., et al. (2008). Absolute physical calibration in the infrared. *The Astronomical Journal*, *135*(6), 2245–2263. https://doi.org/10.1088/0004-6256/135/6/2245

Rieke, M. J., Kelly, D. M., Misselt, K., Stansberry, J., Boyer, M., Beatty, T., et al. (2023). Performance of NIRCam on JWST in flight. *Publications of the Astronomical Society of the Pacific*, *135*(1044), 028001. https://doi.org/10.1088/1538-3873/acac53

Seccull, T., Fraser, W. C., Puzia, T. H., Fitzsimmons, A., & Cupani, G. (2019). 174P/Echeclus and its blue coma observed post-outburst. *The Astronomical Journal*, *157*(2), 88. https://doi.org/10.3847/1538-3881/aafbe4

Sfair, R., & Giuliatti Winter, S. M. (2012). The role of mab as a source for the μ ring of Uranus. *Astronomy and Astrophysics*, *543*, A17. https://doi.org/10.1051/0004-6361/201117346

Showalter, M. (2026). HST analysis notebooks for "characterization of the outer Uranian rings in the visual and near-IR using keck, JWST, and HST observations [Software]. https://doi.org/10.5281/ZENODO.18284982

Showalter, M. R. (1985). *Jupiter's ring system resolved: Physical properties inferred from the voyager images* (Doctoral dissertation). Cornell University. https://doi.org/10.5281/ZENODO.19054369

Showalter, M. R., & Lissauer, J. J. (2006). The second ring-moon system of Uranus: Discovery and dynamics. *Science*, *311*(5763), 973–977. https://doi.org/10.1126/science.1122882

Simon, A. A., Wong, M. H., & Orton, G. S. (2015). First results from the Hubble OPAL program: Jupiter in 2015. *The Astrophysical Journal*, *812*(1), 55. https://doi.org/10.1088/0004-637X/812/1/55

Sumlin, B. J. (2025). *PyMieScatt: Forward and inverse Mie solving routines*. Astrophysics Source Code Library. record ascl:2502.011.

Sumlin, B. J., Heinson, W. R., & Chakrabarty, R. K. (2018). Retrieving the aerosol complex refractive index using pymiescatt: A Mie computational package with visualization capabilities. *Journal of Quantitative Spectroscopy and Radiative Transfer*, *205*, 127–134. https://doi.org/10.1016/j.jqsrt.2017.10.012

van Dam, M. A., Le Mignant, D., & Macintosh, B. A. (2004). Performance of the keck observatory adaptive-optics. *System*, *43*(29), 5458–5467. https://doi.org/10.1364/AO.43.005458

van Dam, M. A., & Macintosh, B. A. (2003). Characterization of adaptive optics at keck observatory. In R. K. Tyson & M. Lloyd-Hart (Eds.), *Astronomical adaptive optics systems and applications* (Vol. 5169, pp. 1–10). https://doi.org/10.1117/12.504223

Warren, S. G., & Brandt, R. E. (2008). Optical constants of ice from the ultraviolet to the microwave: A revised compilation. *Journal of Geophysical Research*, *113*(D14), D14220. https://doi.org/10.1029/2007JD009744

Wizinowich, P. L., Acton, D. S., Lai, O., Gathright, J., Lupton, W., & Stomski, P. J. (2000). Performance of the W.M. keck observatory natural guide star adaptive optic facility: The first year at the telescope. In P. L. Wizinowich (Ed.), *Adaptive optical systems technology* (Vol. 4007, pp. 2–13). https://doi.org/10.1117/12.390368